nature metabolism

ARTICLES

https://doi.org/10.1038/s42255-021-00477-6

Check for updates

The metabolic growth limitations of petite cells lacking the mitochondrial genome

Jakob Vowinckel[1,2,14], Johannes Hartl[1,3,14], Hans Marx[4], Martin Kerick[5,6], Kathrin Runggatscher[1], Markus A. Keller[1,7], Michael Mülleder[1,3,8], Jason Day[9], Manuela Weber[10], Mark Rinnerthaler[10], Jason S. L. Yu[8], Simran Kaur Aulakh[8], Andrea Lehmann[3], Diethard Mattanovich[4], Bernd Timmermann[5], Nianshu Zhang[1], Cory D. Dunn[11,12], James I. MacRae[13], Michael Breitenbach[10] and Markus Ralser[1,3,8] ✉

Eukaryotic cells can survive the loss of their mitochondrial genome, but consequently suffer from severe growth defects. 'Petite yeasts', characterized by mitochondrial genome loss, are instrumental for studying mitochondrial function and physiology. However, the molecular cause of their reduced growth rate remains an open question. Here we show that petite cells suffer from an insufficient capacity to synthesize glutamate, glutamine, leucine and arginine, negatively impacting their growth. Using a combination of molecular genetics and omics approaches, we demonstrate the evolution of fast growth overcomes these amino acid deficiencies, by alleviating a perturbation in mitochondrial iron metabolism and by restoring a defect in the mitochondrial tricarboxylic acid cycle, caused by aconitase inhibition. Our results hence explain the slow growth of mitochondrial genome-deficient cells with a partial auxotrophy in four amino acids that results from distorted iron metabolism and an inhibited tricarboxylic acid cycle.

Mitochondria are crucial organelles, functioning in a range of physiological processes, including metabolism, calcium homeostasis, iron homeostasis and signalling, to the execution of apoptosis[1–6]. In most eukaryotes, mitochondria maintain their own genome, a remnant of their likely α-proteobacterial origin[7–9]. Most genes encoding mitochondrial proteins have been transferred to the nucleus, but important proteins encoded by mitochondrial DNA (mtDNA) remain[7,8]. These are translated in the mitochondrion and are primarily required for the respiratory chain and, in turn, oxidative phosphorylation and a fully functional tricarboxylic acid (TCA) cycle[1,7,8]. Importantly, respiration also drives mitochondrial transport processes by establishing a proton gradient at the inner mitochondrial membrane[1,7,8,10,11].

Some organisms with a mostly parasitic lifestyle have lost the mitochondrial genome and evolved without it[12–14]. Indeed, mtDNA is not under all circumstances essential and its loss can be observed across multiple cell types and species, including human cell lines and yeasts[15,16]. However, cells that tolerate spontaneous loss of mtDNA grow slowly. In yeast, this phenotype has been described more than 70 years ago, and named the 'petite' phenotype, as these slow-growing yeasts form small colonies[17]. Some discoveries made with petites were of historical importance and, for example, led to the discovery of the yeast mitochondrial genome itself[9]. As the research on mitochondrial function is still hindered by difficulties in the manipulation of the sequence of mtDNA[18], petite cells remain an important model to understanding the associated spectrum of physiological roles of mitochondria[9,17,19–32].

The growth defect of petites can be compensated by secondary mutations, which are for instance common in the *Saccharomyces cerevisiae* strain S288C[33], and frequently map to the F_1 subunit of the ATPase (complex V)[21,32,34–38]. Other mutations that affect the F_1 subunit of the ATPase have been associated with thermotolerance[39], or enable species such as *Kluyveromyces lactis* and *Trypanosoma brucei*, where mtDNA is otherwise essential, to survive in its absence[34,40,41].

Despite knowing that the petites lack mtDNA, and that the growth defect can be overcome by specific mutations, it remains unclear which metabolic defects constrain growth. We speculated that elucidating the molecular changes observed in 'evolved' petites would guide us to the underlying defect that restricts growth in 'naive' petites. We first conducted adaptive evolution, and despite lack of mtDNA, petites adapted to near wild-type growth rates by obtaining a set of rapidly and independently occurring mutations in *ATP3*. We then used the isolated suppressor mutations as a tool to identify the metabolic bottlenecks that slow growth. Many cellular processes associated with the function of mitochondria were found to be altered in petites, but not causative for slowing growth. Instead, we find that petites suffer from an insufficient capacity in the biosynthesis of four amino acids: glutamate, glutamine, leucine and arginine. We show that petite cells overcome this defect by bypassing perturbations in

[1]Department of Biochemistry and Cambridge Systems Biology Centre, University of Cambridge, Cambridge, UK. [2]Biognosys AG, Schlieren, Switzerland. [3]Charité – Universitätsmedizin Berlin, Corporate Member of Freie Universität Berlin and Humboldt-Universität zu Berlin, Department of Biochemistry, Berlin, Germany. [4]Department of Biotechnology, University of Natural Resources and Life Sciences Vienna, Vienna, Austria. [5]Sequencing Core Facility, Max Planck Institute for Molecular Genetics and Max Planck Unit for the Science of Pathogens, Berlin, Germany. [6]Institute of Parasitology and Biomedicine 'López-Neyra' (IPBLN, CSIC), Granada, Spain. [7]Institute of Human Genetics, Medical University of Innsbruck, Innsbruck, Austria. [8]The Molecular Biology of Metabolism Laboratory, The Francis Crick Institute, London, UK. [9]Department of Earth Sciences, University of Cambridge, Cambridge, UK. [10]Department of Biosciences, University of Salzburg, Salzburg, Austria. [11]Institute of Biotechnology, Helsinki Institute of Life Science, University of Helsinki, Helsinki, Finland. [12]Department of Molecular Biology and Genetics, Koç University, İstanbul, Turkey. [13]Metabolomics Laboratory, The Francis Crick Institute, London, UK. [14]These authors contributed equally: Jakob Vowinckel, Johannes Hartl. ✉e-mail: markus.ralser@crick.ac.uk

mitochondrial iron metabolism and regaining activity of the TCA cycle at the step of aconitase.

Results

Specific mutations in *ATP3* improve growth of petites. First, we generated mtDNA-deficient petites[42] (ρ^0, opposed to wild-type ρ^+ cells) from a diploid, prototrophic *S. cerevisiae* strain (YSBN1)[43]. We selected clones that formed characteristic small colonies and confirmed loss of mtDNA (Fig. 1a,b). To select mutations that effectively improve growth of cells without mtDNA, petite and wild-type cultures were evolved in a chemostat under glucose-limiting conditions in a highly nutrient-restricted minimal medium (F1)[43]. The cultures were kept under static nutritional conditions for 65 d, during which approximately 352 biomass doublings occurred (Supplementary Fig. 1). Samples were selected, genotyped and phenotyped at regular intervals over time. Large colonies indicative of improved growth in petite cultures were readily apparent at the second sampling point (65 doublings) and became more abundant with time. After 162 doublings, clones forming large colonies dominated all three parallel chemostats (Fig. 1b), while growth of wild-type control cultures remained unaffected (Extended Data Fig. 1).

To identify underlying genetic alterations, we performed whole-genome re-sequencing at the population level (Supplementary Fig. 1; sequenced at generations 0, 260 and 340 for all replicates, and additionally generations 65 and 162 for replicate 3). To rule out secondary (nuclear) mutations caused by mtDNA depletion, we additionally sequenced respective progenitors (Supplementary Table 1). Minority allele detection analysis revealed a specific set of 21 non-synonymous and 30 synonymous mutations that were present in the evolved petites, but not in the ancestral petites or the wild-type cells (Supplementary Table 1). Only mutations in one gene, *ATP3*, enriched over time, and occurred independently between evolution experiments (Fig. 1c and Supplementary Table 1).

We then randomly selected fast-growing colonies of one evolved population (replicate 3) and re-sequenced the *ATP3* locus. This confirmed the three major *ATP3* variants as detected by the population sequencing and revealed three additional *ATP3* mutations with lower prevalence (Supplementary Fig. 2). Each clone contained exclusively one of the identified *ATP3* mutations (Supplementary Fig. 2), indicating that even within one chemostat culture, multiple *ATP3* mutations emerged independently. At the last sampled time point, the majority of cells contained *ATP3* mutations (Fig. 1c, Supplementary Fig. 2 and Supplementary Table 1).

Most uncovered mutations were located at the C-terminal domain of *ATP3* and were closely located to previously isolated petite suppressors[32,35,41,44–46]. This included two mutations that did match residues associated with slow-growth suppression in a petite *S. cerevisiae yme1* mutant (Supplementary Fig. 3a)[35]. All variants affected conserved residues (Supplementary Fig. 3b). Mapping the identified mutations into the structure of complex V highlights a hotspot in a narrow region close to the C terminus of the γ subunit (Fig. 1d and Supplementary Fig. 3).

Importantly, growth rate was significantly increased in isolates with *ATP3* mutations compared with the growth rate of the ancestral petites (Fig. 1e). Transformation of naive petite cells with plasmids harbouring the two most frequent alleles, *ATP3-6* and *ATP3-7* (Supplementary Fig. 3a), as well as an artificial variant that contained both mutations (named *ATP3-6,7*) largely restored growth of petites (Fig. 1f,g). In contrast, the plasmid control and an additional copy of *ATP3* did not compensate for the growth defect in petites (Fig. 1f,g). Similarly, these alleles did not affect growth of wild-type cells (Supplementary Fig. 4). Taken together, mutations within a hotspot region of *ATP3* convey a strong fitness advantage and suppress the petite slow-growth phenotype. As we exclusively isolated *ATP3* alleles during the adaptive evolution experiment that was run in replicates, with a strong selection pressure to optimize growth in minimal F1 medium, over hundreds of generations, and sequenced with high coverage, we conclude that *ATP3* mutations are the most efficient solution to improve growth of petites, at least in the given genetic background and condition.

Mitochondrial membrane potential improved in evolved petites. Strains suppressing the petite phenotype have a more polarized mitochondrial membrane potential ($\Delta\Psi_{mito}$) compared to that of naive petites[29,35,47,48]. Consequently, we examined $\Delta\Psi_{mito}$ in strains carrying newly identified *ATP3* alleles and tested to which extent they relate to the changes in growth rate. Using the *MitoLoc* reporter assay, we monitored differences in $\Delta\Psi_{mito}$ and mitochondrial morphology, between naive and evolved petites, as well as in 'reconstituted' evolved petites heterologously expressing the *ATP3* alleles[49]. Wild-type cells showed colocalization of the MitoLoc markers consistent with a functional $\Delta\Psi_{mito}$[49]. Colocalization was lost in petites, indicating depolarization (Fig. 2a). Expression of the petite-suppressing *ATP3* alleles restored mitochondrial colocalization of the MitoLoc markers, indicating an improvement of $\Delta\Psi_{mito}$ (Fig. 2a). These results were corroborated by a quantitative colocalization analysis[49] (Fig. 2b) and through staining with the $\Delta\Psi_{mito}$-dependent dye 3,3′-dihexyloxacarbocyanine iodide ($DiOC_6$; Fig. 2c and Supplementary Fig. 5). Similarly, *ATP3* mutants isolated from the evolution experiments revealed an increase in $\Delta\Psi_{mito}$, compared with the petite controls (Supplementary Fig. 6a). Overall, we found that the increase in $\Delta\Psi_{mito}$ (Fig. 2b and Supplementary Fig. 6a)

Fig. 1 | *ATP3* variants overcome the slow-growth phenotype of petites. a, Petites lost their mitochondrial genome. Wild-type (left) and petite (right) cells were analysed using DAPI staining ($n = 3$ biological replicates per genotype, c1–c3). In addition to the nucleus, wild-type cells display dot-like structures indicative of mtDNA, which is absent in petites. Scale bars, 1 µm. **b**, Petites with improved growth emerge during adaptive laboratory evolution. Petites grown in chemostats under glucose-limiting conditions were sampled after 65, 162 and 260 generations, and spotted on F1 agar plates. After 260 generations, cultures largely regained the capacity to form larger colonies. Shown is one representative of $n = 3$ biological replicates. **c**, *ATP3* substitutions emerge and their prevalence increases during adaptive laboratory evolution. Relative frequency of the three most abundant heterozygous *ATP3* mutations (*ATP3-6, ATP3-7* and *ATP3-8)* appearing over time in chemostat cultures as estimated from whole-population sequencing. **d**, Molecular context of isolated suppressor mutations in the yeast ATPase complex. Detailed view of F1c10 ATPase structure with α (green), β (turquoise) and γ (grey) subunit interface. Identified mutations (Supplementary Fig. 2) in the γ-subunit are highlighted in red. The small inlet structure shows the entire complex (PDB ID 2XOK[116]) with highlighted γ-subunit (dark grey) and mutations in the C-terminal region (red). **e**, Evolved petite isolates with *ATP3* mutations displayed elevated growth rates. Growth rates of isolates from evolved populations that were genotyped for *ATP3* were recorded in F1 medium with 0.5% glucose. The petite ancestor strain exhibited a significantly lower growth rate compared to that of isolates carrying *ATP3-6, ATP3-7* or *ATP3-8*. Shown are mean values ± s.d. of $n = 4$ (ρ^0 ATP3-6, ρ^0 ATP3-7, ρ^0 ATP3-8 and ρ^0 ATP3-9) or $n = 6$ (ρ^+ and ρ^0) biological replicates per genotype. ΔOD, change in optical density. **f**, Heterologous expression of *ATP3* substitutions increased growth of petites. Wild-type and YSBN11 petites expressing plasmid (pRS313)-based *ATP3* variants were grown in F1 medium with 0.5% glucose. *ATP3* variants significantly improved growth compared with vector controls or wild-type *ATP3*. Mean values ± s.d. of $n = 3$ biological replicates per genotype are shown. *P* values are based on two-sided, unpaired *t*-tests comparing ρ^0 with other genotypes. **g**, Growth curves of wild-type and YSBN11 petites expressing plasmid (pRS313)-based *ATP3* variants as indicated. Shown are fitted models (solid lines) of the mean values (dots) ± s.d. (shaded areas) of $n = 3$ biological replicates per genotype.

correlated with the gain in growth rate (R^2=0.93; Supplementary Fig. 6b), suggesting a link to the restored growth phenotype of evolved petites (Fig. 1e,f).

While mitochondria in unperturbed wild-type yeasts are highly connected, petites exhibit a fragmented mitochondrial network, indicative of mitochondrial fission induced by depolarization of $\Delta\Psi_{mito}$[49,50]. Monitoring mitochondrial morphology using super-resolution microscopy, we tested whether mitochondrial fission in petites is explained by their compromised $\Delta\Psi_{mito}$. However, the mitochondrial network of petites carrying the *ATP3* mutations displayed a similar degree of fragmentation compared with naive petite cells (Fig. 2a and Supplementary Fig. 7), indicating that depolarization of $\Delta\Psi_{mito}$ is not the only cause of mitochondrial fission in petites.

Suppressor mutations improve growth but not biomass of petites. A primary function of the respiratory chain, oxidative ATP biosynthesis, is interrupted in petites. Moreover, it has been hypothesized that, in petites, the remaining and assembled F_1 subunit of the ATP synthase[51] could be running in 'reverse' to hydrolyse mitochondrially imported ATP, and restore $\Delta\Psi_{mito}$ via the electrogenic exchange of mitochondrial ADP^{3-} with cytosolic $ATP4^{-}$[37,40,52–56]. In both scenarios, decreased ATP availability could become growth limiting[31]. However, we found that the energy charge[57] was unaffected

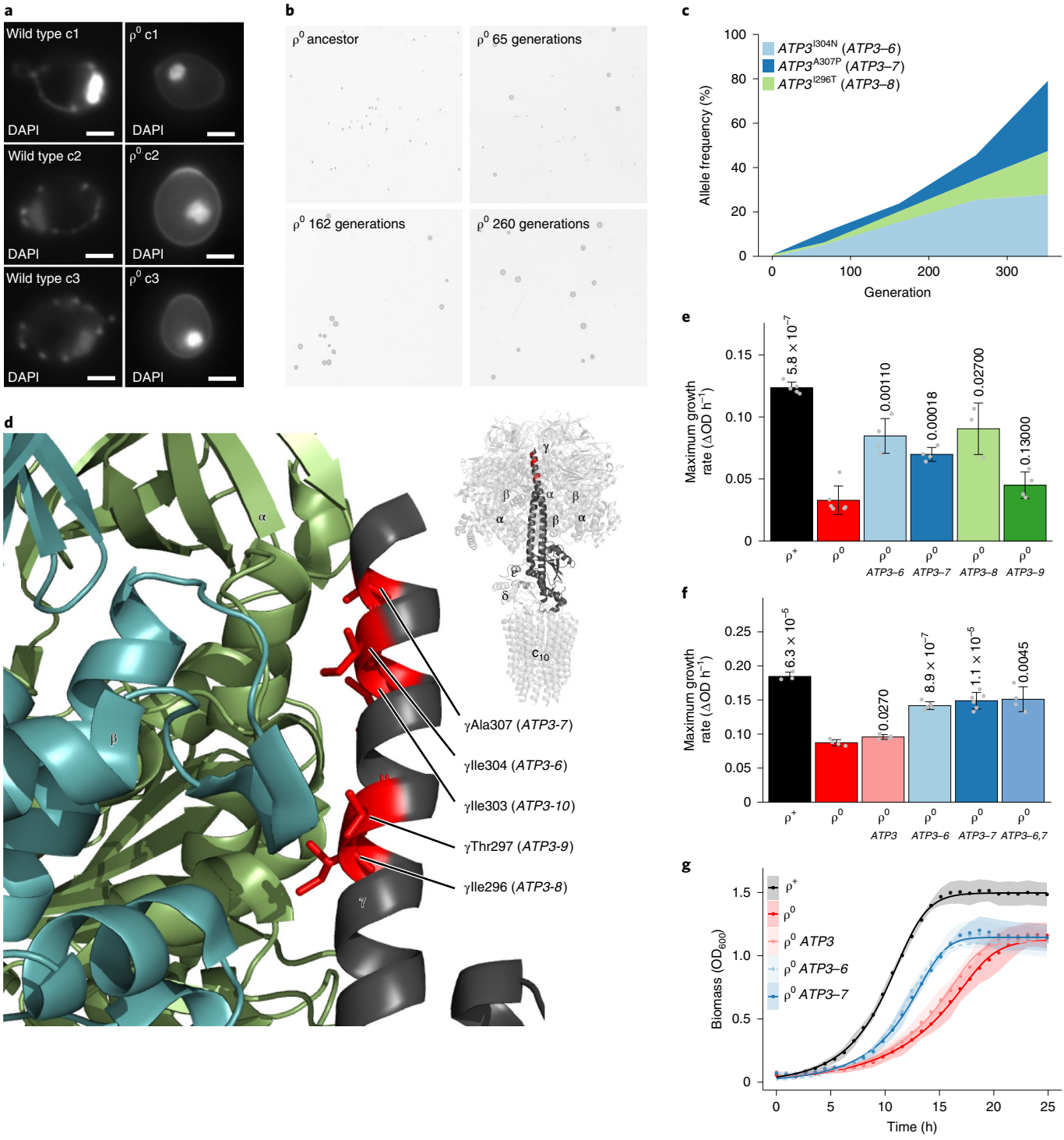

in petites and evolved petites compared to that in wild-type cells (Supplementary Fig. 8). ATP levels in petites only collapsed after glucose exhaustion (Supplementary Fig. 9); in the absence of the respiratory chain, petites cannot consume the remaining non-fermentable substrates, that is, ethanol and glycerol[58]. Further, quantification of the oligomycin-insensitive F1 ATPase activity revealed that it was strongly reduced rather than increased in petites and evolved petites compared to that in wild-type cells (Fig. 2d). Hence, we conclude that the evolution of fast growth in petites is not achieved through altering ATP metabolism, or a futile metabolic cycle in which increased ATP hydrolysis restored the $\Delta\Psi_{mito}$.

Next, we performed fermentation experiments to determine the efficiency of petite and evolved petites in converting glucose into biomass. We determined carbon balances of wild-type cells, petites and evolved petites by measuring glucose uptake, ethanol and glycerol production, steady-state CO_2 and O_2 levels in the bioreactor, as well as the obtained biomass during growth on glucose (Fig. 2e–h and Supplementary Fig. 10). Further, we used the obtained data on glucose consumption, ethanol and glycerol production as well as obtained biomass in a model to estimate physiological parameters such as yield coefficients, growth rates and uptake/excretion rates during the exponential phase of all strains (10.5 h; Supplementary Table 2). The wild-type cells consumed glucose and entered a diauxic shift after 13.9 h, having accumulated 168% of the biomass generated by petites (Fig. 2e). Petite cells reached glucose exhaustion after 20.0 h (Fig. 2f), reflecting their slower growth rate. Strains carrying *ATP3-6* or *ATP3-7* reached the stationary phase and glucose exhaustion considerably faster than petites (15.9 h; Fig. 2e,f). Despite accelerating growth, the *ATP3* adaptations did not largely affect the biomass yield, that is, the biomass produced per glucose consumed (Supplementary Table 2), nor the biomass obtained until the diauxic shift (Fig. 2e) or the ability to consume non-fermentable carbon sources (Fig. 2g,h). Thus, suppressor mutations do not affect these metabolic properties of petites. Instead, we speculated that the growth rate of petites might be compromised because biosynthetic pathways do not meet the required rates to support faster growth.

Four amino acids limit the growth of cells without mitochondrial DNA. To pinpoint the biochemical processes affected in petite cells, we performed untargeted proteomics[59]. The proteomic data indicated that petites suffer from a broad range of metabolic perturbations that revolve around central carbon metabolism, the TCA cycle and amino acid metabolism (Fig. 3a,b). Although a contribution of the TCA cycle was expected due to the loss of crucial components of the respiratory chain[1], the degree of perturbed pathways involved in the biosynthesis of amino acids was somewhat surprising. Curiously, recent findings from *Schizosaccharomyces pombe*, which is normally petite negative, indicated that that supplementation with amino acids derived from α-ketoglutarate supported growth following pharmacological inhibition of the respiratory chain[60]. This supports the hypothesis that, in respiratory-deficient cells, metabolism of α-ketoglutarate and downstream amino acids are challenged[61].

We thus continued with a quantification of amino acids and respective precursors, which confirmed perturbation of intermediary metabolism in petites (Fig. 3b). Petites were characterized by strongly reduced concentrations of leucine and arginine, as well as the arginine precursors citrulline, ornithine and α-ketoglutarate. In parallel, enzymes of the associated synthesis pathways were differentially expressed in petites. Following expression of the mutant *ATP3* alleles, their expression was partially alleviated (Fig. 3b and Supplementary Fig. 11). Curiously, the amino acid levels did not follow these changes and levels remained low in evolved petites compared with wild-type cells (Fig. 3b). We speculated that this result could indicate that the demand for these metabolites was limiting.

Therefore, we conducted supplementation experiments with combinations of leucine and arginine, as well as glutamate and glutamine, which both are directly associated with α-ketoglutarate metabolism. Supplementation of these amino acids, in separation, and specifically in their combination, lead to a disproportionate increase in the growth rate of petites compared with wild-type cells or evolved petites (Fig. 3c and Supplementary Fig. 12). Consistent with previous observations, leucine shortages are particularly growth limiting due to the high biosynthetic requirements for this amino acid[62–64], and leucine accordingly had a particularly strong impact on the growth rate of petites (Fig. 3c). The supplementation of arginine, which has also been described as beneficial to petites in another study[65], but also the combination of glutamine and glutamate further benefited growth of petites. Importantly, these supplementations had a less positive effect on growth in wild-type cells or evolved petites. When supplemented with all four amino acids (QERL) at once, the growth rate differences of petites, evolved petites and wild-type cells became minimal (Fig. 3c–e). Supplementation with all proteinogenic amino acids also accelerated growth, but the complex treatment was less effective than the addition of QERL alone (Fig. 3c). The lower efficacy of the broad supplementation is potentially caused by multiple amino acids competing for the same transporters[66], or by substrate-induced downregulation of amino acid transport in more complex media[67–70]. Lastly, we tested if improved growth by QERL supplementation coincides with an increase in $\Delta\Psi_{mito}$. Indeed, the membrane potential was generally higher in the fast-growing cells. However, differences between wild-type, petite and evolved petite cells overall remained (Supplementary Fig. 13). Taken together, these data

Fig. 2 | Suppressor mutations lead to an increased mitochondrial membrane potential, while morphology and capacity to metabolize glucose remain largely unaffected. a, Indicated strains were transformed with pMitoLoc[49] containing fluorescent proteins with $\Delta\Psi^{mito}$-dependent (preCOX4-mCherry) or $\Delta\Psi^{mito}$-independent (mtGFP) mitochondrial import. Naive petites accumulated cytosolic preCOX4-mCherry, indicating reduced $\Delta\Psi^{mito}$. In contrast, wild-type (ρ^+) and evolved petites (ρ^0) expressing *ATP3* variants showed colocalization of both markers, indicating $\Delta\Psi^{mito}$ polarization. Scale bars, 1 µm. **b**, Quantitative analysis of $\Delta\Psi^{mito}$ estimated from Pearson correlation coefficient (PCC) values of pixel-by-pixel protein colocalization exemplified in **a**. Petites displayed a significant decrease of $\Delta\Psi^{mito}$ compared with wild-type cells, while expression of plasmid-encoded *ATP3* variants improved $\Delta\Psi^{mito}$ in petites. *P* values are based on two-sided, unpaired *t*-tests comparing naive petites to other genotypes (cell numbers as indicated). Mean values ± s.e.m. **c**, Estimation of $\Delta\Psi^{mito}$ in strains described in **a** by $DiOC_6$ staining followed by quantification with flow cytometry of $n = 19{,}956$ (ρ^+), $n = 16{,}104$ (ρ^0), $n = 19{,}112$ (ρ^0 *ATP3-6*) and $n = 18{,}893$ (ρ^0 *ATP3-7*) events. **d**, Mitochondrial ATPase activity is reduced in petites. Both naive and evolved petites showed a significant reduction of the oligomycin-insensitive ATPase activity compared with wild-type cells. Mean values of $n = 5$ biological replicates ± s.e.m. *P* values are based on two-sided, unpaired *t*-tests comparing wild-type to petites and evolved petites. **e**–**h**, The capacity to metabolize glucose was largely unaffected in evolved petites. Indicated genotypes (YSBN11) were cultured in batch fermenters for 45 h in F1 medium containing 2% glucose. Dashed lines indicate the time required to reach the stationary phase. Wild-type cultures accumulated more biomass (OD_{600}; **e**). Only the wild-type cells underwent a diauxic shift and continued to grow. Additionally, glucose (**f**), ethanol (**g**) and glycerol (**h**) levels were monitored over time. Glucose was fully exhausted in all cultures, and ethanol and glycerol are produced. Petites produced higher levels of glycerol compared with the wild-type cells, but were unable to metabolize glycerol or ethanol.

suggest that insufficient rates in the synthesis of specific amino acids, especially of leucine, arginine, glutamine and glutamate, are limiting the growth rate of petites.

Activated retrograde response is not rescuing growth defects. The observation that multiple amino acid biosynthesis pathways were affected indicated that regulatory processes, the cellular chemical

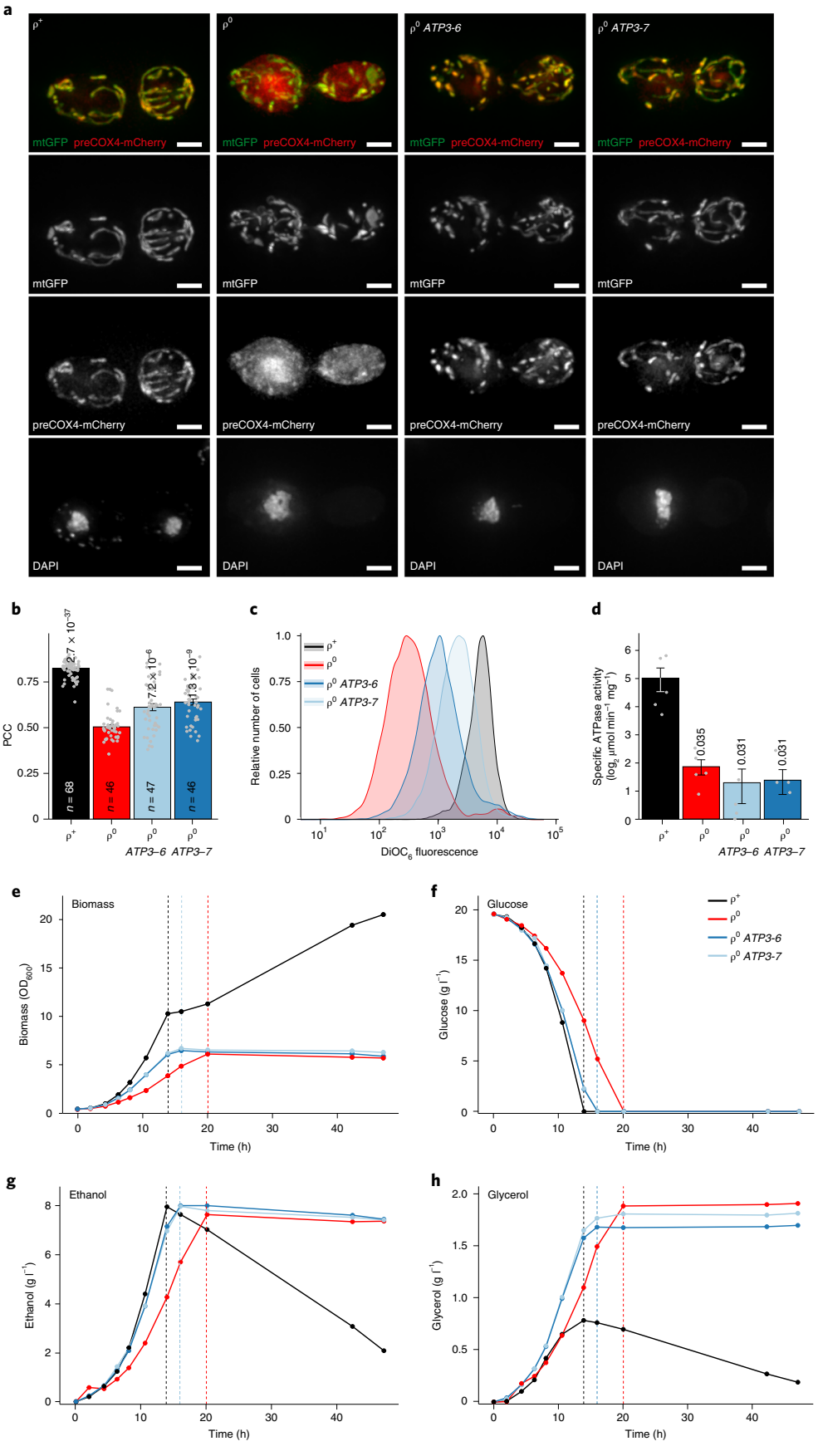

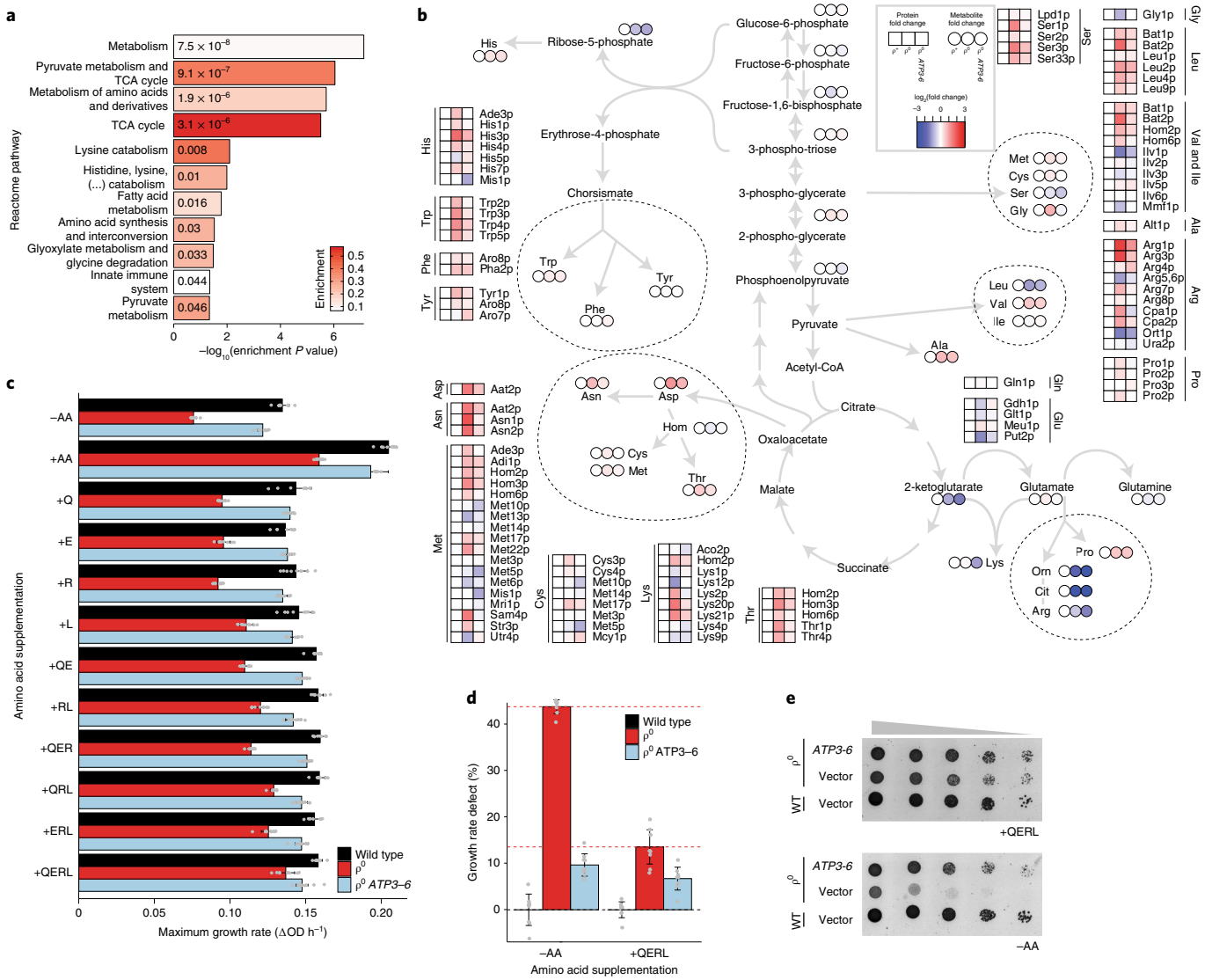

Fig. 3 | Amino acid metabolism is perturbed in petites, and their growth defect is rescued by the addition of selected amino acids. a, Pathway enrichment analysis of proteomics data indicated metabolic defects associated with loss of mtDNA. Differentially expressed proteins between wild-type and naive petites were determined using sequential window acquisition of all theoretical mass spectra (SWATH-MS) and subjected to pathway enrichment analysis using String-db. Eleven reactome pathways were significantly enriched (false discovery rate (FDR) < 5%), with most enriched pathways being biological functions related to TCA cycle and amino acid biosynthesis. Enrichment is represented by bar size ($-\log_{10}$(enrichment *P* value)), bar colours indicate enrichment over background frequency (number of changed proteins compared with all proteins of that pathway). Nine TCA pathway proteins (enrichment = 0.56) were changed in naive petites. Protein abundance data from $n = 4$ biological replicates per genotype. Note that the *P* values stated in the corresponding bar chart represent non-log-transformed values. **b**, Differential expression of proteins and metabolites of naive and evolved petites compared with wild-type cells. A simplified pathway representation of central carbon metabolism in *S. cerevisiae*. Mean fold changes of enzyme (squares) and metabolite levels (circles) of wild-type cells (left column; plasmid control) compared with petites (middle column; plasmid control) and evolved petites (right column, expressing *ATP3-6*). $n = 4$ biological replicates per genotype. **c**,**d**, Supplementation with glutamate, glutamine, arginine and leucine disproportionately benefited petites. Genotypes as described in **b** were grown in synthetic minimal (SM) medium supplemented without (−AA) or with the addition of a mix of proteinogenic amino acids (+AA), or with combinations of glutamate (E), glutamine (Q), arginine (R) and leucine (L; all 2 mM), and OD_{600} was monitored in 96-well cultures. Growth of petites (0.075 OD min^{-1}) increased to 0.137 OD min^{-1} after supplementation with QERL (**c**). The relative growth defect of petite cells (normalized to the percentage growth rate of wild-type cells) was compensated from 43.3% to 13.5% after QERL supplementation (**d**). Mean values ± s.d. of $n = 5$ biological replicates. **e**, Indicated strains were pre-grown in minimal medium ± QERL supplementation. A serial dilution series (1:5 dilutions) was spotted with an initial OD_{600} of 0.5 on agar plates with the indicated media composition. Shown is one of $n = 2$ independent experiments. WT, wild type.

environment or common metabolic precursors, were limiting the growth of petites.

First, we tested if the uncovered amino acid deficiency is associated with perturbed redox metabolism. For instance, when NADPH, which is required for amino acid anabolism and reduction of glutathione (GSH), is limiting, yeast is more sensitive to the oxidant diamide[71–75]. Overall, we detected small differences in diamide sensitivity between strains (Extended Data Fig. 2a). GSH pools were comparable between wild-type and petite strains (Extended Data Fig. 2b–d). Lastly, superoxide levels only marginally changed, but

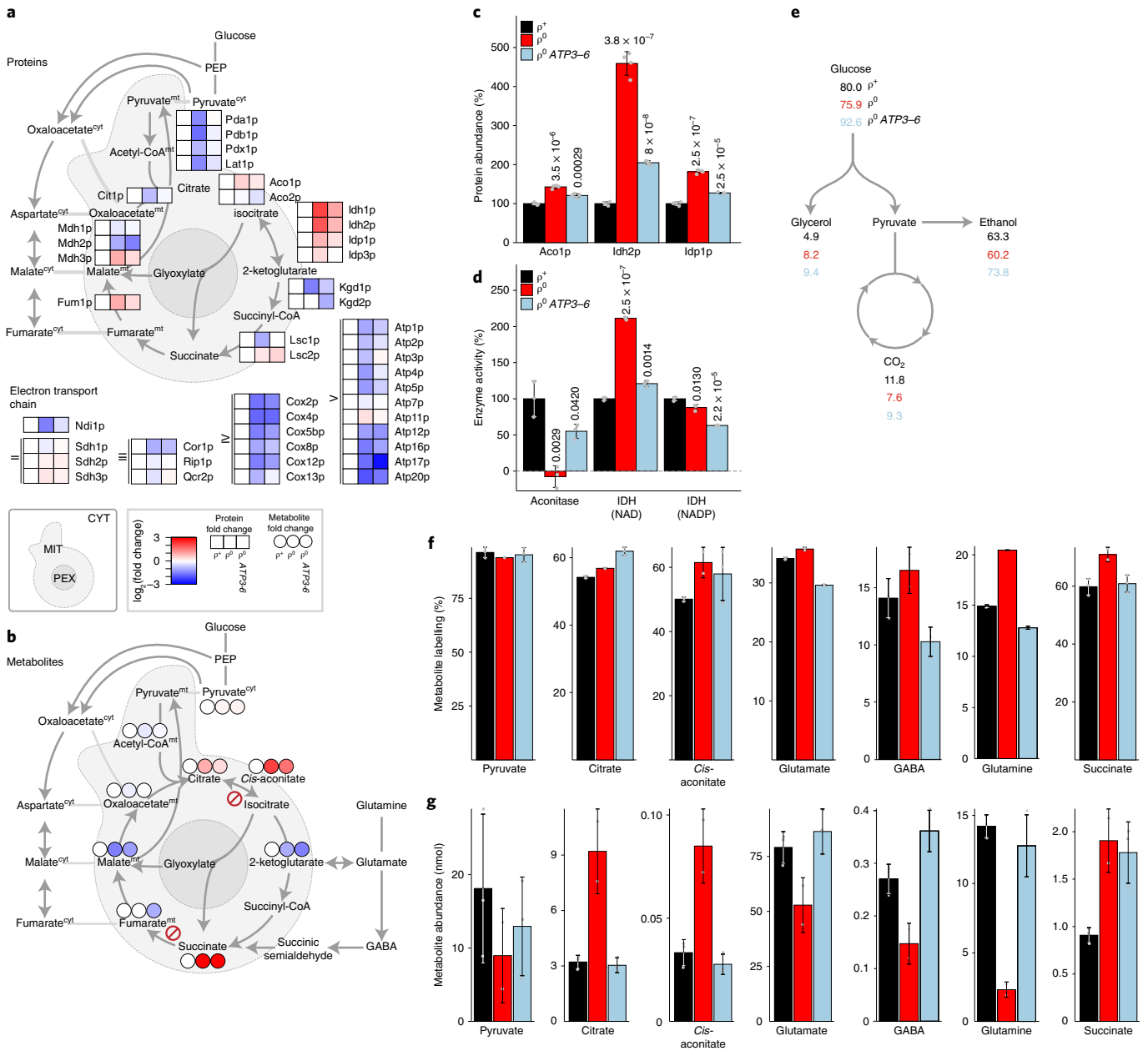

Fig. 4 | Aconitase and tricarboxylic acid cycle are inhibited in petites, which is alleviated in evolved petites. a,**b**, Simplified pathway representation of central carbon metabolism in *S. cerevisiae*. Shaded areas indicate cellular localization (mitochondrial (MIT), peroxisomal (PEX) and cytosolic (CYT)) labelled according to the small inlet. Shown are mean fold changes of protein levels (**a**, squares; $n = 4$ biological replicates) and metabolite levels (**b**, circles; $n = 3$ biological replicates) of wild-type (left column; plasmid control) compared with naive (middle column; plasmid control) or evolved petite (right column; expressing *ATP3-6*) cells. The electron transport chain and SDH are impaired in petites[1,7,8]. PEP, phosphoenolpyruvate. **c**, Levels of the NAD-dependent and NADP-dependent IDH (Idh2p/Idp1p), as well as the major mitochondrial aconitase (Aco1p) were elevated in petites, which partially reverts in evolved petites. Mean values ± s.d. of $n = 4$ biological replicates. *P* values are based on two-sided, unpaired *t*-tests comparing wild-type strain to other genotypes. Data are from **a**. **d**, Enzyme activities from enzyme assays with indicated cell extracts and enzymes. Despite increased expression levels of aconitase (**c**), activity was reduced below the detection limit in petites, but activity was regained in evolved petites. Shown are mean values ± s.d. of $n = 3$ biological replicates per genotype normalized to the wild-type strain. *P* values shown are based on two-sided, unpaired *t*-tests comparing wild-type strain to other genotypes. **e**, Major carbon fluxes in wild-type cells, petites and evolved petites during exponential growth on glucose. Wild-type (top row), petite (middle row) and evolved petite (bottom row) cells were grown in bioreactors (Fig. 1e–h) and fermentation products were monitored. Shown are the estimated carbon-balanced glucose-uptake rates, ethanol and glycerol production rates, as well as the calculated remaining carbon flux allocated to CO_2 that is indicated as the TCA cycle. Indicated rates are given as cmol gDW^{-1} h^{-1}. **f**,**g**, Fractional labelling and pool sizes of pyruvate, TCA cycle, glutamate, glutamine and GABA, monitored during dynamic stable isotope-labelling experiments. Fractional labelling was similar (**f**), while pool sizes of indicated metabolites differed between genotypes (**g**). Naive petites accumulated citrate/*cis*-aconitate, whereas pool sizes of glutamate, glutamine and GABA were reduced. Shown are mean values ± s.d. of $n = 3$ (wild type, evolved petite) and $n = 2$ (petite) biological replicates.

were lower in petites (Extended Data Fig. 2e). Taken together, these results argue against major NADPH shortages or oxidative imbalances as a cause of the amino acid deficiency of petites.

Next, we focused on amino acid sensing/signalling and studied the response to TOR complex 1 inhibition by rapamycin[76]. However, we found that the chemical sensitivity in the form of half maximal inhibitory concentration (IC_{50}) to rapamycin did not differ between petites or wild-type strains (Supplementary Fig. 14).

We then investigated the role of mitochondrial retrograde (RTG) signalling, which has been attributed to mitochondrial dysfunction[1]. In addition to regulating the expression of mitochondrial genes such as those encoding steps in the TCA cycle, the RTG response has been implicated in regulation of peroxisomal processes[2]. As peroxisomal proliferation is associated with mitochondrial deficiency[77], we quantified peroxisomes using a peroxisomal fluorescent marker (Pts1p-GFP). The number of peroxisomes was significantly increased in petites compared to that in wild-type cells (18.5 ± 1.0 versus 13.0 ± 0.6 in wild type; $P < 0.0001$). Moreover, the number of peroxisomes was close to wild-type levels in evolved petites (11.2 ± 0.6; $P = 0.05$; Extended Data Fig. 3a,b). Similarly, differential expression of proteins associated with the RTG regulon, Aco1p, Dld3p, Idh1p, Idh2p and Pyc1p[1,78], was observed in petites, and this response was alleviated in evolved petites (Extended Data Fig. 3c). These results indicated that, as expected, the RTG response is activated in petites[77,78], but surprisingly not in evolved petites. To test whether suppression of retrograde signalling was causally associated with observed amino acid deficiencies, we deleted *RTG2*, the central mediator of the retrograde response, and *CIT2*, a target of a downstream regulated process, the glyoxylate cycle[1]. Deletion of *RTG2* or *CIT2* did not restore petite growth; instead, the growth defect in petites increased. Moreover, *rtg2* and *cit2* mutants did not affect the ability of *ATP3* mutants to suppress the petite phenotype (Extended Data Fig. 3d). These results suggest that activation of the retrograde response pathway is a protective response for cells without mtDNA, but not causing the petite phenotype.

Two reactions of the tricarboxylic acid cycle are inhibited in petites. Retrograde signalling is typically associated with synthesis of α-ketoglutarate and associated amino acids[61]. We therefore focused on the TCA cycle, of which α-ketoglutarate is an intermediate. Quantification of both proteins and metabolites involved in TCA cycle reactions revealed that the upper TCA cycle is severely affected in petites compared with wild-type cells (Fig. 4a,b and Supplementary Figs. 15 and 16). Pathway intermediates including citrate, aconitate and succinate accumulated, whereas the concentration of α-ketoglutarate was reduced (Fig. 4b).

A partial explanation for the perturbation of the TCA cycle in petites involves its connection with the respiratory chain. The loss of the mitochondrial genome deletes Cox1p, Cox2p and Cox3p, which are implicated in electron transport from succinate dehydrogenase (SDH) complex to cytochrome c reductase[1,7,8]. Without a functional SDH complex, and potentially fostered by activation of the glyoxylate shunt, succinate accumulated in petites (Fig. 4b).

While our data are consistent with a loss of SDH activity, they did reveal a second, unexpected perturbation within the TCA cycle (Fig. 4b). Levels of citrate and *cis*-aconitate were increased in petites, while the α-ketoglutarate pool was reduced (Fig. 3b). On the protein level, α-ketoglutarate dehydrogenase (Kgd1p and Kgd2p) and succinyl-CoA ligase (Lsc1p and Lsc2p) were downregulated, while aconitase (Aco1p and Aco2p) and especially isocitrate dehydrogenase (IDH; Idh1p, Idh2p, Idp1p and Idp3p) were upregulated in petites (Fig. 4a,c). Upregulation of aconitase and IDH isomers in petites contrasted with the accumulation of their respective substrates (citrate and *cis*-aconitate). Moreover, levels of enzymes involved in catalysis of citrate to α-ketoglutarate returned to wild-type levels in evolved petites.

These results implied that initial reactions of the TCA cycle could be less active in petites and that respective enzymes are upregulated to compensate. We quantified enzyme activities from wild-type, petite and evolved petite extracts using enzyme assays to monitor substrate conversion (Fig. 4d). NAD-dependent IDH activity was increased in petites according to the increased expression levels of the enzyme (Idh1p and Idh2p; Fig. 4a,c,d). The NADP-dependent IDH activity was unchanged (Fig. 4d). In sharp contrast, despite the increase in aconitase protein expression in petites (Fig. 4c), the activity of this enzyme was reduced below the detection limits of the assay (Fig. 4d). Remarkably, aconitase activity was detected in the evolved petites (Fig. 4d).

We asked whether the inhibition of the TCA cycle enzymes is reflected in lower activity of this pathway. Subtracting the carbon-balanced production rate of the major fermentation products ethanol and glycerol from the glucose uptake rate allowed us to estimate the major carbon fluxes between wild-type, petite and evolved petite cells. Indeed, considering their biomass yield and growth rate, petites channelled more carbon from glucose to ethanol/glycerol, which may suggest that less carbon is allocated to the CO_2-producing TCA cycle (Supplementary Table 2 and Fig. 4e). Then, we performed ^{13}C-tracing experiments to estimate the relative activity of the TCA cycle. We followed incorporation of uniformly labelled 13C [U-^{13}C]glucose to pyruvate, and through the upper TCA cycle to succinate (Fig. 4f,g and Supplementary Fig. 17). Of note, as both metabolomics and a metabolite labelling-based strategy could not distinguish shared pathway intermediates of the mitochondrial TCA cycle with the cytosolic/peroxisomal glyoxylate cycle, these data have to be interpreted as a mix of both signals. Moreover, as a surrogate for α-ketoglutarate, which could not be quantified in petites during tracer experiments (the signals were too diluted by addition of labelling), we analysed label incorporation into and pool sizes of glutamate, glutamine and GABA as downstream metabolites. While labelling incorporation after 30 min was largely similar, the substrate levels of aconitase, citrate and *cis*-aconitate were elevated. Instead, the downstream metabolites—glutamate, glutamine and GABA—were reduced in petites, but not in evolved petites (Fig. 4f,g). Especially considering that petites apparently have less overall carbon flux (Fig. 4e), these data are consistent with a reduced activity of reactions towards glutamate, glutamine and GABA, specifically in petites. In contrast, succinate levels were elevated in petites but also in evolved petites (Fig. 4b,g), which is in line with the loss of SDH activity in all strains lacking mtDNA. In summary, aconitase, IDHs and the glyoxylate shunt, targets of the retrograde response, are upregulated in petites. Petites are further characterized by strong reduction in aconitase and SDH activity, while evolved petites overcome the former inhibition.

Loss of mitochondrial DNA increases iron levels and inhibits aconitase. Next, we addressed mechanisms that could inhibit aconitase in petites. Aconitase is a prominent iron–sulfur cluster (ISC)-dependent enzyme[79]. Defects of mtDNA and $\Delta\Psi_{mito}$ have been implicated with perturbed iron and ISC homeostasis[30,80–82], and we speculated that this could explain the loss of aconitase activity. First, we investigated the iron regulome[83,84] by recording proteomes of cells depleted and repleted with iron (Fig. 5a,b). To distinguish confounding effects caused by the differences in growth rate, we applied principal-component analysis (PCA, Extended Data Fig. 4). Growth rate (PC1) and iron-depletion (PC2) response were the two dominant drivers of proteome changes. Growth rate-sensitive proteins (PC1) changed substantially in petites, but not in wild-type cells and evolved petites (Fig. 5a). Instead, the top 50 iron-response proteins (PC2) changed according to iron depletion in all wild-type, petite and evolved petite cells (Fig. 5b). This includes proteins expected to change in response to iron depletion, such as ISC proteins that are downregulated after iron starvation[85] (Fig. 5b and

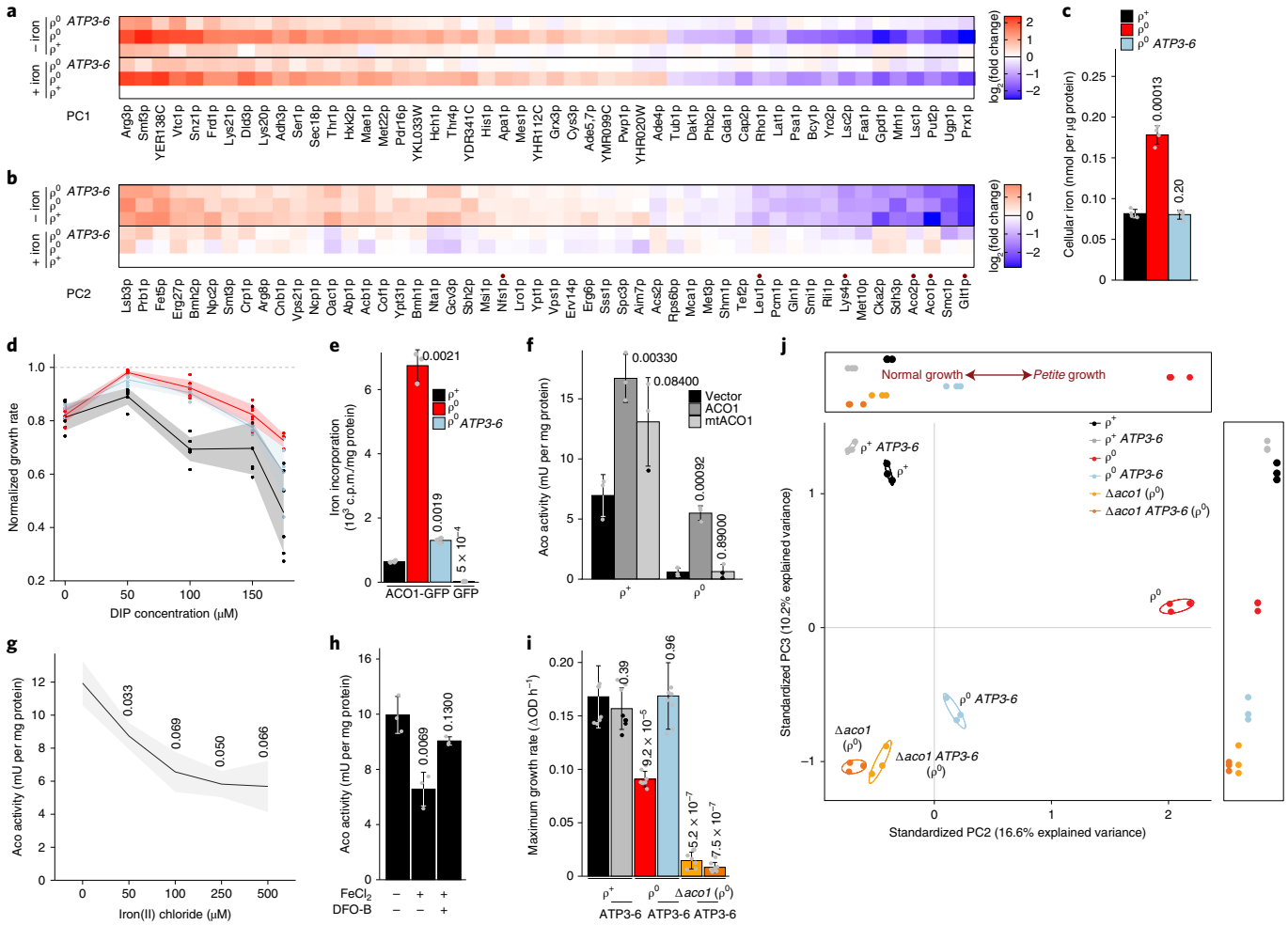

Fig. 5 | Iron overload inhibits aconitase, which is required for petite suppression. a,**b**, The iron starvation response was activated in petites. Proteomics of wild-type/petite cells ($n = 4$ biological replicates) grown with or without iron supplementation as analysed by PCA (Extended Data Fig. 4). Heat maps show respective top 50 proteins with highest loadings in PC1 (**a**) and PC2 (**b**). While proteins in PC1 (growth rate) were upregulated in petites independent of iron addition, proteins in PC2 (iron response) changed irrespective of genotype. Red dots indicate ISC proteins. **c**, Increased intracellular iron levels in petite cells compared with wild-type and evolved petite cells. Ions were quantified by ICP–MS and normalized to protein content. Mean values ± s.d. of $n = 3$ biological replicates. **d**, Petites were more resistant to iron depletion as estimated from dose-response curves of strains listed in **c**. Shown is the normalized growth rate against increasing concentrations of the iron chelator dipyridyl (DIP). Growth rate was normalized to the maximum growth rate obtained with physiological iron concentrations of the respective genotypes (dashed line). Shown are mean values (solid lines) ± s.d. (shaded area) of $n = 6$ biological replicates. **e**, Aco1p binds excessive iron in naive petites. BY4741 wild-type, petite and evolved petite cells all expressing Aco1-GFP were exposed to ^{55}Fe, and binding to isolated Aco1-GFP was quantified. Mean values ± s.d. of $n = 3$ biological replicates. **f**, Mitochondrial aconitase activity was reduced in petites. Wild-type and petite BY4741 yeast expressing plasmid controls, plasmids harbouring native ACO1 or *ACO1* fused to an additional mitochondrial targeting sequence (*mtACO1*). Aconitase activity was detected in wild-type cells and increased following heterologous expression of *ACO1/mtACO1*. In petites, aconitase activity was only detected by heterologous expression of native ACO1. Mean values ± s.d. of $n = 3$ biological replicates. **g**, Aconitase was sensitive to increasing iron levels in vitro. Shown is the activity of wild-type extracts challenged with increasing concentrations of iron(II) chloride; mean values (line) ± s.d. (shaded area) of $n = 3$ independent replicates. **h**, Iron-dependent aconitase inhibition was alleviated by iron chelation. Genotypes and set-up as in **g**. Cell extracts were incubated ±100 µM iron(II) chloride and treated ±20 mM DFO-B and aconitase activity determined. Addition of 100 µM iron significantly reduced aconitase activity, which was alleviated by DFO-B. Mean values ± s.d. of $n = 3$ independent replicates. **i**,**j**, Petites no longer benefited from *ATP3-6* expression after deletion of aconitase. The slow-growth phenotype of petites was amplified and could not be rescued in cells in a Δ*aco1* background (**i**). Mean values ± s.d. of $n = 3$ biological replicates. Similarly, the proteome profile of Δ*aco1* did not respond to *ATP3-6* expression (**j**). Proteomics followed by PCA with normalized intensities of all proteins. Proteome profiles of wild-type cells clustered together, while those of slow-growing and fast-growing petites were separated along PC2. In contrast, Δ*aco1* was not separated from Δ*aco1* expressing *ATP3-6*. Data from $n = 3$ biological replicates. Statistics are based on unpaired, two-sided *t*-tests comparing wild-type strain with other genotypes (**c**, **e**, **f** and **i**) or comparing treated with untreated controls (**g** and **h**).

Supplementary Fig. 18) or iron transporters that are upregulated (Supplementary Fig. 18). Thus, petites mount a functional response to iron depletion.

Next, we tested for perturbed ion homeostasis, and conducted a total elemental composition analysis to quantify a range of elements, including iron, in wild-type cells and petites by inductively coupled plasma–mass spectrometry (ICP–MS; Supplementary Table 3). We found iron levels were significantly elevated (>twofold) in petites compared with those in wild-type cells. Other element concentrations were not affected. (Fig. 5c and Supplementary Table 3).

Strikingly, iron levels returned to those of wild-type cells afer expression of *ATP3-6* (Fig. 5c).

To investigate whether iron was associated with petite cell growth defects, we added iron chelators to the medium, and the growth rate of wild-type cells dropped with increasing iron chelator concentrations. Relative to their reduced growth rate, petites tolerated iron depletion slightly better (Fig. 5d and Supplementary Fig. 19). To test if aconitase might be directly affected by elevated iron levels in petites, we supplemented the cells with the radioactive iron isotope ^{55}Fe and affinity-purified mitochondrial Aco1p-GFP. Protein-bound iron from immuno-purified Aco1p-GFP was quantified by scintillation counting. Aconitase enriched from wild-type cells showed weak radioactivity. Instead, aconitase purified from petites bound a high degree of radioactivity (Fig. 5e). We then heterologously overexpressed *ACO1*, which is localized in both cytoplasm and mitochondria[86]. Furthermore, we overexpressed *ACO1* fused with an additional mitochondrial targeting signal[49]. In a wild-type background, aconitase activity was detected, and overexpression of both *ACO1* constructs increased aconitase activity consistently (Fig. 5f). Instead, in petite extracts, aconitase activity was reduced to the detection limit of the assay. Moreover, no increase in total aconitase activity was detected when the overexpressed protein was additionally targeted to mitochondria in petites (Fig. 5f).

Aconitase activity could be low because of faulty folding/assembly with ISCs. Furthermore, a principally functional enzyme could be sensitive to high iron levels. Thus, we tested aconitase activity in vitro in wild-type extracts with increasing iron concentration. Aconitase was active; however, the activity decreased with increasing iron concentrations (Fig. 5g). Adding the iron chelating agent deferoxamine (DFO-B) prevented this effect (Fig. 5h). Nonetheless, wild-type aconitase retained a higher activity in the presence of iron compared with aconitase purified from petites (Fig. 5g,f). These results imply that two scenarios apply: aconitase purified from petites is dysfunctional and binds excessive iron (Figs. 4d and 5e,f) and a per se functional aconitase is sensitive to increased iron levels (Fig. 5g,h).

These findings suggested that aconitase itself would be required to suppress the petite phenotype. Thus, we generated an *aco1* deletion strain, which loses respiratory function and mtDNA (Supplementary Fig. 20a)[87], and is auxotrophic for glutamate (Supplementary Fig. 20b). This is in line with perturbation of the TCA cycle reactions towards α-ketoglutarate[88]. Likewise, growth of petites further deteriorated after deletion of *aco1* (Fig. 5i). Based on classification with PCA, petites with intact *ACO1* have a strong shift along PC2 after expression of *ATP3-6* (Fig. 5j and Supplementary Fig. 21). This effect was abolished following *aco1* deletion from petites, indicating that the suppressor mutation *ATP3-6* lost its function when aconitase was disabled (Fig. 5j). Moreover, petite *Δaco1* cells expressing *ATP3-6* could no longer suppress the slow-growth phenotype (Fig. 5i). Thus, a functional aconitase is required for petite suppression, and the inhibition of the TCA cycle is directly associated with the slow-growth phenotype of petites.

Discussion

The loss of mtDNA in yeast causes a severe growth defect described in 1949 as the petite phenotype. The molecular basis of this phenotype has never been fully clarified[17]. Mitochondria are major organelles implicated in many cellular processes[1–6] and the loss of the mitochondrial genome accordingly has broad physiological consequences. To pinpoint the factors slowing growth of petites, we used adaptive evolution. Remarkably, accelerated growth of petites was readily evolved and explained by mutations located in a narrow region of the ɣ subunit of the complex V. Mutations in this hotspot are known as one of the most common substitutions in the yeast genome[32,35,41,44,45]. We recently provided evidence that the frequent occurrence of such mutations coincides with an increase in the spontaneous mutation frequency in petites[32]. Here we find that the selective advantage of *ATP3* alleles is provided by improving growth in petites and that mutations in this gene are a major solution to overcome the petite phenotypes. In petites, the *ATP3* mutations are dominant and, similarly to previously isolated mutant alleles, restore the mitochondrial membrane potential. However, our results argue against futile metabolic cycles to underlie the restoration of the $\Delta\Psi_{mito}$ because biomass formation does not change with petite suppression. It is thus possible that the isolated variants are gain-of-function mutations that generate a so-far unknown biochemical activity. Although additional work will be required to elucidate the mechanistic details, it is sensible to assume that elevated $\Delta\Psi_{mito}$ benefits mitochondrial functionality and hence various processes involving mitochondria, such as mitochondrial protein import and homeostasis[10,89].

In this study, we focused on the physiology of evolved petites and used them to identify growth-limiting factors of cells without mtDNA. We used the basic assumption that perturbing the mechanism that was 'repaired' in evolved mutants would leave the otherwise dominant allele dysfunctional. This strategy is illustrated by ruling out the RTG response as a cause of the slow-growth phenotype. We find that the RTG response is activated following loss of the mitochondrial genome and mitigated in evolved petites. Moreover, deletion of crucial components of the RTG response amplified the growth defects in petites. Further, the selected *ATP3* alleles could still improve growth of petites in which the RTG response was disrupted. Activation of the RTG response is hence beneficial to petites as a downstream protective response, but cannot explain the growth benefit of isolated suppressor mutations.

Eventually, our data converged in a model in which petites grow slowly because they are unable to synthesize sufficient amounts of selected amino acids. We then continued to identify underlying molecular mechanisms. We discover that the TCA cycle in petites, which supplies biosynthetic precursors, or shares metabolites and ISC enzymes with affected pathways, is interrupted at two enzymatic steps, SDH and aconitase. While SDH activity is generally lost in petites[1,7,8], evolved petites overcome aconitase inhibition. Strikingly, once aconitase is deleted, the *ATP3* mutations lose their function.

We suggest that two mechanisms affect aconitase in petites. First, aconitase binds excessive iron in petites, and increased levels of iron inhibit even an otherwise functional aconitase. Second, our and previous findings argue that in petites ISC assembly and export is perturbed due to a reduction of $\Delta\Psi_{mito}$[30,80–82]. Reduced export of ISC proteins can in turn explain elevated mitochondrial iron levels and contribute to incorrect loading of ISCs[80].

All four amino acids that we uncovered to benefit petites rely on at least partial mitochondrial biosynthesis[90,91]. Glutamate synthesis, required for production of glutamine and arginine, depends on α-ketoglutarate. Leucine synthesis requires Acetyl-CoA and is inhibited by CoA[90,92]. Another common denominator in the biosynthesis of these amino acids is their requirement for ISCs, specifically in the case of leucine (*ILV3* and *LEU1*) and glutamate/glutamine (*GLT1*)[80,81,90]. Nevertheless, as petites are viable, there must be residual assembly and loading of ISCs. Notably, yeast is particularly sensitive to perturbations in leucine metabolism, which is a frequently encoded amino acid and needs to be synthesized at high rates, and the strong growth defect of leucine auxotrophs cannot fully be compensated by supplementation[62–64]. It seems plausible that a shortage in ISC metabolism would manifest in the leucine pathway, not only because it is in high demand, intertwined with the Krebs cycle and mitochondrial metabolism, but also because it depends on mitochondrial ISC export[93].

Taken together, while numerous cellular processes depend on mitochondria, the main growth rate restriction caused by loss of mtDNA is explained by a specific biosynthetic defect in amino

acid metabolism that roots in a distorted mitochondrial iron homeostasis. This defect can be largely overcome by nutritional supplementation.

Methods

Statistics and reproducibility. Statistical analysis was performed using unpaired, two-sided *t*-tests in R unless indicated otherwise. Comparisons with $P < 0.05$ were considered significantly different. No statistical method was used to predetermine sample size and no data were excluded from the analysis. Only measurements using liquid chromatography coupled with mass spectrometry (LC–MS) were randomized. Microscopy image acquisition was performed in such a way that the investigator was blinded for sample identity. For other experiments, investigators were not blinded to allocation during experiments and outcome assessment.

Chemicals and media. All chemicals were obtained from Sigma-Aldrich unless stated otherwise. Prototrophic yeast strains were cultured in SM medium, consisting of 6.8 g l^{-1} yeast nitrogen base (YNB, Sigma), or F1 medium[43]. Auxotrophic strains were supplemented with 20 mg l^{-1} histidine, 60 mg l^{-1} leucine, 20 mg l^{-1} uracil, 20 mg l^{-1} methionine and/or 50 mg l^{-1} lysine or 5 mM glutamate as indicated. Synthetic complete medium was prepared by supplementing SM medium with CSM-HIS-LEU-MET-TRP-URA (MP Bio), 10 mg l^{-1} adenine, 20 mg l^{-1} uracil, 40 mg l^{-1} tryptophan and amino acids listed in the preceding sentence. YP medium consists of 20 g l^{-1} peptone (Bacto) and 10 g l^{-1} yeast extract (Bacto). Cultivation in iron-depletion conditions was performed in YNB without amino acids and without iron (Formedium), and analytical-grade EMSURE H_2O (Merck). Where indicated, this medium was supplemented with 200 µg l^{-1} $FeCl_3 \times 6\times H_2O$. Media were supplemented with 2% glucose unless stated otherwise. Media were solidified using 2% agar (Difco).

Yeast strains. Adaptive evolution was performed with wild-type YSBN1, a prototrophic diploid variant of *S. cerevisiae* S288c[43]. For transformation with plasmid constructs, derivatives of YSBN1 with single deletions of *ura3* or *his3* were used[43]. Where indicated, BY4741 was used. Single-gene deletion mutants BY4741 *Δcit2*, *Δzwf1* and *Δrtg2* were obtained from the yeast deletion collection[94] and identity was verified by sequencing. BY4741 *Δaco1* was generated by inserting a natMX targeting cassette[95] into the *ACO1* locus, which was verified by sequencing.

Strains depleted of mtDNA (ρ^0) were generated by plating yeast on YPD agar containing 0.1 g l^{-1} ethidium bromide followed by incubation at 30 °C for 2 d. Absence of mtDNA was confirmed in isolated clones by DAPI staining and absence of growth on glycerol. For petites carrying a plasmid, single clones were subjected to the mtDNA depletion procedure as described above after transformations and counter selection.

Plasmid constructs. Plasmids used in this study are listed in Supplementary Table 4 and are available via Addgene. For construction of various pRS313_ATP3 plasmids, respective *ATP3* variants (T911A, G919C, T911A and G919C) were first obtained by PCR site-directed mutagenesis. Resulting alleles and the respective native promoter region (the ~600-bp upstream region) were sub-cloned using the pGEM-T System (Promega). Subsequently, respective *ATP3* alleles (including wild type) were cloned into the multiple cloning site of pRS313 (ref. [96]) by digests with SalI/BamHI. Successful insertion was evaluated using blue/white selection. Finally, Sanger sequencing confirmed the respective *ATP3* alleles of pRS313-ATP3 constructs and excluded additional mutations. Plasmid expressing Aco1p-GFP has been described in Klinger et al.[97] and plasmid expressing GFP-Pts1 was a gift from E. Hettema[98]. The *mtACO1* construct was created by addition of preSu9 sequence using homologous recombination and insertion into p416GPD using BamHI/SalI sites.

Adaptive evolution and genome sequencing. Wild-type and petite cells were cultured in F1 carbon-limited medium[99] with 2.5 g l^{-1} glucose as the carbon source in a DASGIP Parallel Bioreactor Systems chemostat for 67 d, with pH controlled at 4.5, agitation at 200 r.p.m. and temperature at 30 °C. Three chemostat cultures were grown for each genotype at a dilution rate of 0.1. Cryo stocks were sampled daily and stored in 25% glycerol at −80 °C.

For genome sequencing, sampled cryo stocks were regrown in 5 ml YPD and 1.4 ml were collected in the exponential phase. Genomic DNA was extracted with a Wizard Genomic DNA Purification Kit (Promega) according to the manufacturer's protocol.

Whole-genome sequencing was performed on an Illumina HiSeq 2500 platform with 50-bp paired-end sequencing. The adaptor sequence was AAT GATACGGCGACCACCGAGATCTACACTCTTTCCCTACACGACGCTCT TCCGATCT. Data were analysed according to Schweiger et al.[100]. To this end, 96% of reads could be aligned against the database 'Saccharomyces_cerevisiae. EF4.69.dna_sm.toplevel.fa' obtained from Ensembl using the Burrows–Wheeler Aligner (BWA, v.0.5.9-r16)[101] after sequencing adaptor removal; duplicates were marked using Picard 'MarkDuplicates' and coverage was between 61× and 452×. Single-nucleotide polymorphism calling was done after local realignment using 'UnifiedGenotyper' from the GATK v.2.2 pipeline with default (sensitive) parameters. Annotation was done using ANNOVAR[102] with information from Ensembl *Saccharomyces cerevisiae* v69. Positions with coverage below 10× in any of the experiments were excluded from the analysis, as well as positions that were mutated in any of the wild-type time points as found in >1% of reads with a minimum of two reads. Suppressor mutations of petites were included if they were found in >1% of reads with a minimum of two reads at the final time point of at least one culture.

Growth curves and chemostat experiments. *Determination of growth rates.* For determination of growth rates, yeast was inoculated at an optical density (OD_{600}) ~ 0.1 in the respective liquid medium in 96-well plates and cultured in a FLUOstar OPTIMA plate reader (BMG LABTECH) for 40 h at 30 °C, with recording of OD_{600} every 20 min. Growth rate and lag phase were both determined from growth curves using a Richards model fit from the R 'grofit' package (v.1.1.1-1)[103].

Chemostat experiments and quantification of fermentation products. In total, 200 ml pre-culture medium (10 g l^{-1} yeast extract (Merck), 20 g l^{-1} soy peptone (Kerry Bio-Science) and 22 g l^{-1} glucose monohydrate (Roth) were inoculated with 750 µl cryostock of the respective yeast strains and grown on an orbital shaker at 30 °C and 180 r.p.m. overnight. This culture was used for inoculation of the bioreactors at an OD_{600} of 0.4. The batch cultivations were performed in 1.4-l bioreactors (DASGIP Parallel Bioreactor System) with 1.0 l F1 medium containing 2% glucose. Cultivation temperature was controlled at 30 °C, pH was controlled at 5.0, and the dissolved-oxygen concentration was maintained above 20% saturation by controlling the stirrer speed between 200 and 1,200 r.p.m., as well as the airflow between 6 sl h^{-1} to 40 sl h^{-1}. Inlet and outlet gases were followed by the off-gas sensor provided by the bioreactor system (DASGIP Off-Gas Analyzer GA4, DASGIP AG). Foam formation was prevented by the automatic addition of a 1% solution of Struktol SB2121 (Schill + Seilacher).

Next, 12 ml of culture was sampled at regular intervals, and OD_{600} was determined using a spectrophotometer (Ultrospec 1100pro, Amersham Biosciences). A correlation between the OD_{600} and the cell dry mass was established. The concentrations of glucose, glycerol and ethanol in the culture broth were determined by HPLC analysis (Shimadzu) with a Phenomenex Rezex ROA column (300 mm × 7.8 mm) and a refractive index detector (RID-10A, Shimadzu). The column was operated at 60 °C, 1 ml min^{-1} flow rate and 4 mM H_2SO_4 as a mobile phase. HPLC samples were prepared by adding 100 µl of 40 mM H_2SO_4 to 900 µl culture supernatant. Subsequently, the samples were filtered on 0.20-µm RC membrane filters and 10 µl was injected for analysis. Rates for glucose uptake, ethanol and glycerol production, as well as growth rate, were estimated by fitting the time courses (including time points up to 10.5 of growth) to an ordinary differential equation model assuming exponential growth and constant yield. The model is detailed in work by Litsios et al., and gPROMS Model Builder (v.4.0, Process Systems Enterprise Ltd) was used for parameter estimation. For carbon balancing, stoichiometric production of 1 mol of CO_2 per 1 mol of ethanol was assumed[104].

Microscopy. *Quantification of mitochondrial membrane potential and morphology by MitoLoc.* Microscopic analysis of $\Delta\Psi^{mito}$ was carried out using the MitoLoc system[49]. In short, cells transformed with pMitoLoc were washed and resuspended in formaldehyde solution. Cells were embedded in Vectashield mounting medium and analysed using an Olympus IX81 wide-field microscope (Deltavision, GE Healthcare) equipped with a ×60 1.42-NA PlanApoN oil objective (Olympus) and an LED light source capable of delivering 405-nm, 488-nm and 594-nm excitation wavelengths. The filter sets used were FITC (excitation at 490/20 nm and emission at 528/38 nm), TRITC (excitation at 555/28 nm and emission at 617/73 nm) and DAPI (excitation at 360/40 nm and emission at 457/50 nm), and images with a *z*-spacing of 200 nm were recorded with a CoolSNAP HQ2 CCD camera. Deconvolution was performed using Softworx (GE Healthcare). For standard fluorescence microscopy, cells were examined under an Olympus BX51 microscope using filters YGFP (GFP) and HcRed1 (mCherry). Pixel-by-pixel colocalization of preSU9-GFP and preCOX4-mCherry was used as a measure for $\Delta\Psi^{mito}$ using the Pearson correlation coefficient[49]. Mitochondrial fragmentation analysis using super-resolution microscopy was determined essentially as described previously[49] using a Deltavision 3D-SIM OMX system (GE Healthcare) equipped with a ×100 1.4-NA oil objective (Olympus), 405-nm, 488-nm and 594-nm laser lines, and the OMX Standard filter set drawer. Images were acquired in structured illumination mode using a *z*-spacing of 125 nm and reconstructed using Softworx.

Quantification of mitochondrial membrane potential with $DIOC_6$. Strains were grown in an SM medium for 4 h to an OD_{600} of ~0.5. A total of 5×10^6 cells were stained with 175 nM $DiOC_6$ in HEPES with 5% glucose for 15 min at 30 °C. After washing with PBS, cells were resuspended in fresh medium, embedded in agarose pads and subjected to microscopy[49], using excitation/emission wavelengths of 488/528 nm. For $DIOC_6$ analysis using flow-cytometry, freshly streaked colonies were resuspended in 30 µl H_2O and 10 µl of suspension was used to inoculate 500 µl SM medium or SM medium with 2 mM glutamate, glutamine, arginine and leucine (+QERL) and incubated overnight with agitation at 30 °C. The following day,

cultures were diluted at a ratio of 1:2 and cultured for another 4–8 h to an OD_{600} of ~0.5. Cells were then spun down at 3,200*g* for 3 min and the medium exchanged with SM medium or SM medium + QERL supplemented with 175 nM $DiOC_6$, incubated at 30 °C with agitation for a further 15 min. Cells were then re-pelleted and washed with 500 µl PBS per well, before final centrifugation and resuspension in 500 µl PBS. In total, 200 µl of each culture was transferred to a U-bottomed 96-well plate and taken for high-throughput flow cytometry analysis on a Fortessa X20 HTS cytometer. Acquisition parameters were 120 µl sample injection at a flow rate of 1 µl s^{-1}. $DiOC_6$ fluorescence was captured using 488-nm blue laser excitation followed by a 530/30 band-pass filter.

Quantification of peroxisomes. The number of peroxisomes was determined in GFP-Pts1p-expressing BY4741 yeast using super-resolution microscopy as described above. In short, BY4741-expressing GFP-Pts1p was cultured to exponential phase in SC-HU medium containing 2% glucose, harvested by centrifugation, washed twice in PBS and fixed by resuspension in formaldehyde solution (4 g l^{-1} paraformaldehyde and 3.6% sucrose). The number of peroxisomes was counted using CellProfiler (v.2.0)[105].

Reactive oxygen species quantification. Reactive oxygen species (ROS) production was assessed by growing strains in SM medium for 4 h to an OD_{600} of ~0.5. Where indicated, cells were pre-treated with 2 mM tert-butyl-hydroperoxide for 5 min to induce formation of ROS, and 5×10^6 cells stained with 2.5 µg ml^{-1} dihydroethidium for 5 min in the dark. After washing with PBS, cells were resuspended in fresh medium, embedded in agarose pads and subjected to microscopy as described above, using excitation/emission wavelengths of 510/595 nm. Images were analysed using CellProfiler (2.0)[105], counting the proportion of cells with detectable fluorescence.

Metabolomics and proteomics. *Metabolomics.* Respective yeasts were grown to mid-log phase and biomass corresponding to 10 ml of OD_{600} of 0.75 was harvested by injection into cold methanol. The pellet was collected (2 min, 4,000*g*, 4 °C), and metabolites were extracted with glass beads and a FastPrep device[73].

Measurements were performed with a triple-quadrupole mass spectrometer (Agilent 6460) coupled to a HPLC Agilent 1290 instrument operating in selective reaction monitoring mode. Respective metabolites were identified by specific retention time and fragmentation pattern as obtained from analytical standards. Peaks were identified and integrated with Masshunter Workstation (Agilent) and metabolites were quantified by external calibration.

Glycolytic and pentose phosphate pathway intermediates[73], as well as AMP/ADP/ATP[106] were separated on a Zorbax C8 SB-C8 Rapid Resolution HD, 2.1 × 100 mm, 1.8-µm column (Agilent). Mobile phase was a mixture of buffer A (10% acetonitrile) and buffer B (50% acetonitrile) with 750 mg l^{-1} octylammonium acetate. The flow rate was 0.6 ml min^{-1}. A total of 1 µl of sample was injected and separated with 5% buffer B, ramped to 70% over 2.5 min, then 80% for 0.5 min, followed by equilibration with 5% buffer B and the needle was washed before each injection. For more details, see work by Campbell et al.[73].

Amino acids were separated by hydrophilic interaction liquid chromatography with an Acquity UPLC BEH-amide column (Waters, 1.7 µm; 2.1 × 100 mm at a flow rate of 0.9 ml min^{-1}. Mobile phase was a mixture of solvents A (50:50, acenonitrile:water) and solvent B (95:5:5, acetonitrile:methanol:water); both were buffered with 10 mM ammonium formate and acidified with 0.176% formic acid. Then, 1 µl sample was injected and separated with 85% buffer B for 0.7 min, ramped to 5% over 1.85 min, kept at 5% for 0.2 min before returning to starting conditions and equilibration for 0.65 min. For more details, see work by Mülleder et al.[107].

Reduced and oxidized glutathione (GSH and GSSH, respectively) were separated using a binary gradient with 0.1% formic acid in H_2O as buffer A and methanol as buffer B. Separation was achieved by isocratic flow at 100% A at 0.5 ml min^{-1} for 0.5 min, which was then ramped to 10% B within 2.5 min. After a 0.5-min washing step at 10% B, the column was re-equilibrated to 100% A resulting in a total cycle time of 5 min. GSSG and GSH were quantified in positive electrospray ionization mode via the multiple reaction monitoring transitions: 613 → 484, 613 → 355, 613 → 231 (fragmentor: 120, collision energy: 18), and 308 → 233, 308 → 179, 308 → 161 (fragmentor: 105, collision energy: 9), respectively. Medium glucose was quantified using LC–MS/MS according to the study by Mülleder et al.[108] modified by including the transition 179 → 89 (70 V fragmentor, 5 V collision energy, negative mode).

Protein profiling, data analysis and pathway enrichment. For protein profiling, single colonies of the respective yeast strains were grown to mid-log phase in selective medium containing 2% glucose, collected by centrifugation and snap frozen in aliquots equalling 10 ml of OD_{600} of 1. Cells were broken by bead shaking with 200 µl 0.05 M ammonium bicarbonate in a FastPrep (3 × 30 s, 6.5 m s^{-1}, 4 °C), and cell pellet after centrifugation was re-extracted with 200 µl lysis buffer (0.1 M NaOH, 0.05 M EDTA, 2% SDS and 2% 2-mercaptoethanol) for 10 min at 90 °C, and again for 10 min at 90 °C after addition of 0.1 M acetic acid. Combined supernatants were precipitated using 10% TCA, and processed further according to the RapiGest protocol. Protein concentration was adjusted to 2 µg µl^{-1} with 0.2% RapiGest SF (Waters) in ABC. Before analysis, samples were spiked with 0.5 × HRM kit (Biognosys). SWATH LC–MS/MS analysis was performed according to Vowinckel et al.[59]. Briefly, samples were acquired on a TripleTOF 5600 instrument (SCIEX) hyphenated to a nanoACQUITY chromatographic system (Waters) operating at a 3 µl min^{-1} flow rate. Data were analysed with Spectronaut (v.14, Biognosys AG) and post-processed in R. PCA was carried out using the unfiltered dataset and the 'prcomp' function. Protein fold change was calculated with reference to the wild-type strain, and differential abundance was defined as a fold change > 1.5 and FDR-corrected *P* value < 0.01. Pathway enrichment was performed in String-db (v.11)[109], and Reactome pathways[110] were reported as significantly enriched if the FDR-corrected enrichment *P* value < 0.05.

Dynamic labelling experiments. *Sample preparation.* For dynamic labelling experiments, yeast cultures were inoculated at an OD_{600} of 0.15 in F1 medium containing 2% glucose and agitated at 30 °C until reaching mid-log phase. Then, 45 ml of an OD_{600} of 1 (~6×10^8 cells) were pelleted, resuspended in 6 ml F1 medium containing 1 % (wt/vol) [U-$^{13}C_6$]glucose (Cambridge Isotope Laboratories) and kept at 30 °C with occasional agitation. Next, 1 ml of cells (~1×10^8 cells) was removed after 1, 5, 15 and 30 min, shock frozen by injection into 20 ml of −40 °C methanol and pelleted by centrifugation (2 min, 4,000*g*, 4 °C). Supernatant was removed, and metabolites were extracted in 600 µl chloroform:methanol (600 µl, 2:1 vol/vol), transferred to a 1.5-ml tube, followed by sonication in a water bath for 1 h at 4 °C. Samples were pelleted by centrifugation (10 min, 16,000*g*, 4 °C), the supernatant was collected, and the pellet re-extracted with methanol:water (600 µl, 2:1 vol/vol, containing 1 nmol *scyllo*-inositol). Samples were pelleted (10 min, 16,000*g*, 4 °C), corresponding samples were pooled, and dried in a rotary vacuum concentrator. Samples were biphasic partitioned by addition of 100 µl chloroform, followed by 600 µl methanol:water (1:1 vol/vol) and vigorous vortexing. After centrifugation (as above), the upper (polar) phase was removed, dried and processed for gas chromatography–mass spectrometry (GC–MS; see below).

Gas chromatography–mass spectrometry. Polar metabolites were derivatized and analysed by GC–MS (Agilent 7890B-5977A), and identification and abundance of individual metabolites was estimated according to McRae et al.[111]. In brief, dried metabolite samples were washed with methanol (twice), and derivatized overnight at room temperature (RT) with methoxyamine (20 mg ml^{-1} in pyridine; Sigma) followed by addition of BSTFA + 1% TMCS (Sigma) for >1 h at RT. GC–MS was performed using splitless injection (injection temperature 270 °C) onto a 30 m + 10 m × 0.25 mm DB-5MS + DG column (Agilent J&W), with helium carrier gas, in electron impact ionization mode. The oven temperature was initially 70 °C (2 min), followed by an increase to 295 °C at 12.5 °C per minute and subsequently to 320 °C at 25 °C per minute (held for 3 min). GAVIN[112] was used for metabolite identification and quantification by comparison to the retention times, mass spectra and responses of known amounts of authentic standards.

Iron-depletion experiments and ^{55}Fe incorporation binding assays. *Iron depletion for proteomics.* Culture was performed by inoculating a pre-culture (iron-depleted SM medium with or without iron, 2% glucose) with washed yeast cells and incubation overnight at 30 °C. Main culture was inoculated to an OD_{600} of 0.1 and incubated at 30 °C with shaking until cultures reached an OD_{600} of 0.7. Biomass corresponding to 10 ml of an OD_{600} of 1 were collected by centrifugation, washed with iron-depleted H_2O and stored at −80 °C.

Iron depletion in liquid medium. Single colonies of indicated strains were transferred to 10 ml of SM medium situated in Erlenmeyer flasks and incubated overnight. Cultures were diluted to an OD_{600} of ~0.2 and incubated for 5 h. Cells were collected, supernatants were discarded and cells were washed three times in sterile H_2O, and OD_{600} was adjusted to 0.2. Then, 5 µl of each culture was transferred to a Microtiter plate with 195 µl of minimal medium with iron, without iron, and without iron and increasing DIP concentration. The base formulation of this medium corresponds to 6.7 g l^{-1} YNB (Sigma Y0626) with 2% glucose. For iron depletion, the ferric chloride was omitted and, where indicated, DIP was added from 50 mM stock dissolved in DMSO to a final concentration of 50, 100, 150 and 175 µM. Growth curves were obtained on a Spark-Stacker (Tecan) plate reader using the mean values of five multi-well reads with OD_{600} obtained every 30 min. Growth rates were estimated from obtained growth data using the spline fit implemented in the R package grofit (v.1.1.1-1).

^{55}Fe incorporation assay. Quantification of ISC formation was performed according to work by Molik et al.[113]. Briefly, BY4741 transformed with pUG35_Aco1 construct were verified for mitochondrial GFP expression using fluorescence microscopy, and pre-cultured overnight in iron-depleted SM + LMW medium with 2% glucose. The main culture was inoculated to an OD_{600} of ~0.1 and grown to mid-exponential phase (30 °C). Cells were collected by centrifugation, washed once with analytical-grade H_2O, resuspended in 10 ml fresh medium per 0.5 g wet cell mass, and incubated for 10 min (30 °C, 200 r.p.m.). Next, 10 µCi $^{55}FeCl_3$ (Perkin Elmer) in 100 µl 0.1 M sodium ascorbate was added to each sample, and iron incorporation was performed for 2 h. After collecting cells by centrifugation

(3,000*g*, 5 min), pellet was washed once with 10 ml citrate buffer (50 mM sodium citrate, 1 mM EDTA, pH 7.0) and once with 1 ml HEPES-KOH (pH 7.4). Cells were disintegrated by bead shaking in a FastPrep device (MP Biomedicals) with 500 µl TNETG + PI buffer (20 mM Tris-HCl (pH 7.4), 2.5 mM EDTA, 150 mM NaCl, 10% (wt/vol) glycerol, 0.5% (wt/vol) Triton X-100, 1× cOmplete Protease Inhibitor Cocktail (Roche)) and 0.5 volume of acid-washed glass beads for 30 s at a speed of 25 per second. After centrifugation (10 min, 17,000*g*, 4 °C), the protein concentration of supernatants was determined, adjusted to 15 µg µl^{-1} and GFP-Aco1p enriched using 25 µl washed GFP-Trap magnetic beads (ChromoTek). Samples were inverted (1 h, 4 °C), beads collected and washed extensively with TNETG + PI buffer. Bound $^{55}FeCl_3$ was quantified by scintillation counting.

Inductively coupled plasma–mass spectrometry. For quantification of elemental composition, yeast cells were resuspended in 4.5 ml analytical-grade H_2O, and proteins were cleaved by addition of 1.4 ml concentrated HNO_3 (final concentration 16.4%) and incubation for 2 h at 80 °C. Following centrifugation (10 min, 4,000*g*), supernatants were analysed in triplicate using ICP–MS on a Perkin Elmer Elan DRC II instrument. The instrument was calibrated by dilution of iron standard solution series (1 ppb (parts per 10^9) to 1 ppm), which was reanalysed at every 16 samples to correct for instrumental drift. A 1-ppb solution of internal standards (In, Re and Rh) was used. Concentrations of elements were normalized to the protein concentration of yeast lysate as determined by BCA assays.

Biochemical and molecular biology assays. *Rapamycin sensitivity testing.* For rapamycin sensitivity assay, strains were inoculated at an OD_{600} of 0.1 with 11 rapamycin concentrations from 50 pg ml^{-1} to 1 µg ml^{-1} ($n = 3$) in a 384 multi-well plate (70 µl per well) in SC-H medium, and growth was monitored for 48 h. The maximum specific growth rate and EC_{50} values for dose-response curves were determined with the R package grofit (v.1.1.1-1).

Yeast dilution spot tests. For oxidant spot tests, a 2 ml overnight culture of yeast was prepared. Cells were collected, washed once in H_2O and resuspended in fresh, autoclaved H_2O to an OD_{600} of 2.5, unless otherwise indicated. Then, 200 µl of the resulting suspension was transferred to a 96-well plate and a 1:5 dilution series was prepared. Oxidant plates were prepared freshly by cooling medium containing agar to ~50 °C, and 1.2 mM diamide was added to aliquots, mixed, cast into petri dishes and cooled to RT. Cell suspensions were vigorously mixed, and 5 µl of each dilution was spotted onto agar plates. Spots were air-dried under a flow hood and incubated at 30 °C for 2–3 d.

For amino acid supplementation spot tests, overnight cultures of indicated strains were prepared in 15 ml SM medium situated in flasks, and supplemented with or without indicated amino acids. The overnight culture was diluted at a 1:20 ratio in respective media and incubated for 5 h. Cells were collected, set to an OD_{600} of 0.5 in the respective media, and spotted and incubated as described above.

For iron-depletion spot tests, the indicated strains were pre-grown in SM medium with 2% glucose. A serial dilution series (1:5) was spotted with an initial OD_{600} of 0.5 on SM medium agar plates with or without 1 mM ferrozine.

Quantification of enzyme activities. IDH activity was quantified using a coupled diaphorase assay[114], using 20 µg ml^{-1} yeast lysate and 2 mM NAD^+ or 2 mM $NADP^+$. The reaction was started by addition of 16 mM isocitrate and followed continuously in 96-well plates at 340 nm in a plate reader (Tecan Infinite 200 PRO). Aconitase activity was quantified via an enzyme assay[97], with 1 U ml^{-1} IDH1 (Roche), 0.4 mM $NADP^+$ and 20 µg ml^{-1} yeast lysate. The reaction was started by addition of 2 mM citrate and absorption at 340 nm was followed continuously. ATPase activity was quantified by initially isolating yeast mitochondria using differential centrifugation and spheroblast formation. Then, a ubiquinol:cytochrome c oxidoreductase (complex III) activity assay was performed[115], and specific activity (µmol ADP per mg protein per minute) of the oligomycin-insensitive fraction was calculated according to the Beer–Lambert law equation.

Aconitase overexpression and localization tagging. Wild-type and petite BY4741 was transformed with a plasmid expressing ACO1, mtACO1 or the empty vector. Cells were grown to mid-exponential phase in SC-U medium, collected, extracted and aconitase activities were determined.

Reporting Summary. Further information on research design is available in the Nature Research Reporting Summary linked to this article.

Data availability

Proteomic data are provided in PRIDE under accession number PXD011715. A list of mass spectrometry files is provided in Supplementary Table 5. Processed metabolomics and proteomics data are provided in Supplementary Data 1–3. There is no restriction on data availability.

Code availability

Code used for data analysis and creation of figures is available at https://github.com/JakobV/metabolic-growth-limitations-of-petite-cells/.

Received: 2 July 2020; Accepted: 10 September 2021;
Published online: 18 November 2021

References

1. Liu, Z. & Butow, R. A. Mitochondrial retrograde signaling. *Annu. Rev. Genet.* **40**, 159–185 (2006).
2. Chelstowska, A. & Butow, R. A. RTG genes in yeast that function in communication between mitochondria and the nucleus are also required for expression of genes encoding peroxisomal proteins. *J. Biol. Chem.* **270**, 18141–18146 (1995).
3. Lill, R. & Mühlenhoff, U. Maturation of iron–sulfur proteins in eukaryotes: mechanisms, connected processes, and diseases. *Annu. Rev. Biochem.* **77**, 669–700 (2008).
4. Saraste, M. Oxidative phosphorylation at the fin de siècle. *Science* **283**, 1488–1493 (1999).
5. Eisenberg, T., Büttner, S., Kroemer, G. & Madeo, F. The mitochondrial pathway in yeast apoptosis. *Apoptosis* **12**, 1011–1023 (2007).
6. Giorgi, C., Marchi, S. & Pinton, P. The machineries, regulation and cellular functions of mitochondrial calcium. *Nat. Rev. Mol. Cell Biol.* **19**, 713–730 (2018).
7. Foury, F., Roganti, T., Lecrenier, N. & Purnelle, B. The complete sequence of the mitochondrial genome of *Saccharomyces cerevisiae*. *FEBS Lett.* **440**, 325–331 (1998).
8. Anderson, S. et al. Sequence and organization of the human mitochondrial genome. *Nature* **290**, 457–465 (1981).
9. Schatz, G., Haslbrunner, E. & Tuppy, H. Deoxyribonucleic acid associated with yeast mitochondria. *Biochem. Biophys. Res. Commun.* **15**, 127–132 (1964).
10. Dunn, C. D. & Jensen, R. E. Suppression of a defect in mitochondrial protein import identifies cytosolic proteins required for viability of yeast cells lacking mitochondrial DNA. *Genetics* **165**, 35–45 (2003).
11. Mitchell, P. Coupling of phosphorylation to electron and hydrogen transfer by a chemi-osmotic type of mechanism. *Nature* **191**, 144–148 (1961).
12. Karnkowska, A. et al. A eukaryote without a mitochondrial organelle. *Curr. Biol.* **26**, 1274–1284 (2016).
13. Tovar, J. et al. Mitochondrial remnant organelles of *Giardia* function in iron–sulphur protein maturation. *Nature* **426**, 172–176 (2003).
14. Zubáčová, Z. et al. The mitochondrion-like organelle of *Trimastix pyriformis* contains the complete glycine cleavage system. *PLoS ONE* **8**, e55417 (2013).
15. Hashiguchi, K. & Zhang-Akiyama, Q.-M. Establishment of human cell lines lacking mitochondrial DNA. *Methods Mol. Biol.* **554**, 383–391 (2009).
16. Nagley, P. & Linnane, A. W. Mitochondrial DNA deficient petite mutants of yeast. *Biochem. Biophys. Res. Commun.* **39**, 989–996 (1970).
17. Ephrussi, B., Hottinguer, H. & Tavlitzki, J. Action de l'acriflavine sur les levures. I. La mutation 'petite colonie'. *Ann. Inst. Pasteur* **76**, 351–367 (1949).
18. Patananan, A. N., Wu, T.-H., Chiou, P.-Y. & Teitell, M. A. Modifying the mitochondrial genome. *Cell Metab.* **23**, 785–796 (2016).
19. Slonimski, P. *La formation des enzymes respiratoires chez la levure* (Desoer, 1953).
20. Ephrussi, B. & Hottinguer, H. Direct demonstration of the mutagenic action of euflavine on baker's yeast. *Nature* **166**, 956 (1950).
21. Chen, X. J. & Clark-Walker, G. D. The petite mutation in yeasts: 50 years on. *Int. Rev. Cytol.* **194**, 197–238 (2000).
22. Mounolou, J.-C. & Lacroute, F. Mitochondrial DNA: an advance in eukaryotic cell biology in the 1960s. *Biol. Cell* **97**, 743–748 (2005).
23. Corneo, G., Moore, C., Sanadi, D. R., Grossman, L. I. & Marmur, J. Mitochondrial DNA in yeast and some mammalian species. *Science* **151**, 687–689 (1966).
24. Mounolou, J. C., Jakob, H. & Slonimski, P. P. Mitochondrial DNA from yeast 'petite' mutants: specific changes in buoyant density corresponding to different cytoplasmic mutations. *Biochem. Biophys. Res. Commun.* **24**, 218–224 (1966).
25. Tewari, K. K., Vötsch, W., Mahler, H. R. & Mackler, B. Biochemical correlates of respiratory deficiency. VI. Mitochondrial DNA. *J. Mol. Biol.* **20**, 453–481 (1966).
26. Rabinowitz, M. & Swift, H. Mitochondrial nucleic acids and their relation to the biogenesis of mitochondria. *Physiol. Rev.* **50**, 376–427 (1970).
27. Nass, M. M. The circularity of mitochondrial DNA. *Proc. Natl Acad. Sci. USA* **56**, 1215–1222 (1966).
28. Garipler, G., Mutlu, N., Lack, N. A. & Dunn, C. D. Deletion of conserved protein phosphatases reverses defects associated with mitochondrial DNA damage in *Saccharomyces cerevisiae*. *Proc. Natl Acad. Sci. USA* **111**, 1473–1478 (2014).
29. Garipler, G. & Dunn, C. D. Defects associated with mitochondrial DNA damage can be mitigated by increased vacuolar pH in *Saccharomyces cerevisiae*. *Genetics* https://doi.org/10.1534/genetics.113.149708 (2013).
30. Veatch, J. R., McMurray, M. A., Nelson, Z. W. & Gottschling, D. E. Mitochondrial dysfunction leads to nuclear genome instability: a link through iron–sulfur clusters. *Cell* **137**, 1247–1258 (2009).

31. Day, M. Yeast petites and small colony variants: for everything there is a season. *Adv. Appl. Microbiol.* **85**, 1–41 (2013).
32. Li, J. et al. Slow growth and increased spontaneous mutation frequency in respiratory-deficient afo1^{-} yeast suppressed by a dominant mutation in *ATP3*. *G3* **10**, 4637–4648 (2020).
33. Goffeau, A. et al. Life with 6,000 genes. *Science* **274**, 563–567 (1996).
34. Chen, X. J., Hansbro, P. M. & Clark-Walker, G. D. Suppression of ρ^0 lethality by mitochondrial ATP synthase F_1 mutations in *Kluyveromyces lactis* occurs in the absence of F_0. *Mol. Gen. Genet.* **259**, 457–467 (1998).
35. Weber, E. R., Rooks, R. S., Shafer, K. S., Chase, J. W. & Thorsness, P. E. Mutations in the mitochondrial ATP synthase gamma subunit suppress a slow-growth phenotype of *yme1* yeast lacking mitochondrial DNA. *Genetics* **140**, 435–442 (1995).
36. Wang, Y., Singh, U. & Mueller, D. M. Mitochondrial genome integrity mutations uncouple the yeast *Saccharomyces cerevisiae* ATP synthase. *J. Biol. Chem.* **282**, 8228–8236 (2007).
37. van Leeuwen, J. et al. Exploring genetic suppression interactions on a global scale. *Science* **354**, aag0839 (2016).
38. Puddu, F. et al. Genome architecture and stability in the *Saccharomyces cerevisiae* knockout collection. *Nature* **573**, 416–420 (2019).
39. Caspeta, L. et al. Biofuels. Altered sterol composition renders yeast thermotolerant. *Science* **346**, 75–78 (2014).
40. Dean, S., Gould, M. K., Dewar, C. E. & Schnaufer, A. C. Single point mutations in ATP synthase compensate for mitochondrial genome loss in trypanosomes. *Proc. Natl Acad. Sci. USA* **110**, 14741–14746 (2013).
41. Schnaufer, A., Clark-Walker, G. D., Steinberg, A. G. & Stuart, K. The F_1–ATP synthase complex in bloodstream stage trypanosomes has an unusual and essential function. *EMBO J.* **24**, 4029–4040 (2005).
42. Goldring, E. S., Grossman, L. I., Krupnick, D., Cryer, D. R. & Marmur, J. The petite mutation in yeast. Loss of mitochondrial deoxyribonucleic acid during induction of petites with ethidium bromide. *J. Mol. Biol.* **52**, 323–335 (1970).
43. Canelas, A. B. et al. Integrated multilaboratory systems biology reveals differences in protein metabolism between two reference yeast strains. *Nat. Commun.* **1**, 145 (2010).
44. Chen, X. J. & Clark-Walker, G. D. Specific mutations in alpha- and gamma-subunits of F_1–ATPase affect mitochondrial genome integrity in the petite-negative yeast *Kluyveromyces lactis*. *EMBO J.* **14**, 3277–3286 (1995).
45. Caspeta, L. & Nielsen, J. Thermotolerant yeast strains adapted by laboratory evolution show trade-off at ancestral temperatures and preadaptation to other stresses. *mBio* **6**, e00431 (2015).
46. Clark-Walker, G. D., Hansbro, P. M., Gibson, F. & Chen, X. J. Mutant residues suppressing ρ^0 lethality in *Kluyveromyces lactis* occur at contact sites between subunits of F_1–ATPase. *Biochim. Biophys. Acta* **1478**, 125–137 (2000).
47. Kominsky, D. J. & Thorsness, P. E. Expression of the *Saccharomyces cerevisiae* gene *YME1* in the petite-negative yeast *Schizosaccharomyces pombe* converts it to petite-positive. *Genetics* **154**, 147–154 (2000).
48. Kominsky, D. J., Brownson, M. P., Updike, D. L. & Thorsness, P. E. Genetic and biochemical basis for viability of yeast lacking mitochondrial genomes. *Genetics* **162**, 1595–1604 (2002).
49. Vowinckel, J., Hartl, J., Butler, R. & Ralser, M. MitoLoc: a method for the simultaneous quantification of mitochondrial network morphology and membrane potential in single cells. *Mitochondrion* **24**, 77–86 (2015).
50. Rapaport, D., Brunner, M., Neupert, W. & Westermann, B. Fzo1p is a mitochondrial outer membrane protein essential for the biogenesis of functional mitochondria in *Saccharomyces cerevisiae*. *J. Biol. Chem.* **273**, 20150–20155 (1998).
51. Schatz, G. Impaired binding of mitochondrial adenosine triphosphatase in the cytoplasmic 'petite' mutant of *Saccharomyces cerevisiae*. *J. Biol. Chem.* **243**, 2192–2199 (1968).
52. Klingenberg, M. & Rottenberg, H. Relation between the gradient of the ATP/ADP ratio and the membrane potential across the mitochondrial membrane. *Eur. J. Biochem.* **73**, 125–130 (1977).
53. Giraud, M. F. & Velours, J. The absence of the mitochondrial ATP synthase delta subunit promotes a slow growth phenotype of ρ- yeast cells by a lack of assembly of the catalytic sector F_1. *Eur. J. Biochem.* **245**, 813–818 (1997).
54. Buchet, K. & Godinot, C. Functional F1–ATPase essential in maintaining growth and membrane potential of human mitochondrial DNA-depleted rho degrees cells. *J. Biol. Chem.* **273**, 22983–22989 (1998).
55. Clark-Walker, G. D. Kinetic properties of F_1–ATPase influence the ability of yeasts to grow in anoxia or absence of mtDNA. *Mitochondrion* **2**, 257–265 (2003).
56. Smith, C. P. & Thorsness, P. E. Formation of an energized inner membrane in mitochondria with a gamma-deficient F_1–ATPase. *Eukaryot. Cell* **4**, 2078–2086 (2005).
57. Atkinson, D. E. The energy charge of the adenylate pool as a regulatory parameter. Interaction with feedback modifiers. *Biochemistry* **7**, 4030–4034 (1968).
58. Merz, S. & Westermann, B. Genome-wide deletion mutant analysis reveals genes required for respiratory growth, mitochondrial genome maintenance and mitochondrial protein synthesis in *Saccharomyces cerevisiae*. *Genome Biol.* **10**, R95 (2009).
59. Vowinckel, J. et al. Cost-effective generation of precise label-free quantitative proteomes in high-throughput by microLC and data-independent acquisition. *Sci. Rep.* **8**, 4346 (2018).
60. Malecki, M., Kamrad, S., Ralser, M. & Bähler, J. Mitochondrial respiration is required to provide amino acids during fermentative proliferation of fission yeast. *EMBO Rep.* **21**, e50845 (2020).
61. Liu, Z. & Butow, R. A. A transcriptional switch in the expression of yeast tricarboxylic acid cycle genes in response to a reduction or loss of respiratory function. *Mol. Cell. Biol.* **19**, 6720–6728 (1999).
62. Alam, M. T. et al. The metabolic background is a global player in *Saccharomyces* gene expression epistasis. *Nat. Microbiol.* **1**, 15030 (2016).
63. Mülleder, M. et al. A prototrophic deletion mutant collection for yeast metabolomics and systems biology. *Nat. Biotechnol.* **30**, 1176–1178 (2012).
64. Tsuji, J. et al. The frequencies of amino acids encoded by genomes that utilize standard and nonstandard genetic codes. *Bios* **81**, 22–31 (2010).
65. Druseikis, M., Ben-Ari, J. & Covo, S. The Goldilocks effect of respiration on canavanine tolerance in *Saccharomyces cerevisiae*. *Curr. Genet.* **65**, 1199–1215 (2019).
66. Regenberg, B., Düring-Olsen, L., Kielland-Brandt, M. C. & Holmberg, S. Substrate specificity and gene expression of the amino acid permeases in *Saccharomyces cerevisiae*. *Curr. Genet.* **36**, 317–328 (1999).
67. Ruiz, S. J., van't Klooster, J. S., Bianchi, F. & Poolman, B. Growth inhibition by amino acids in *Saccharomyces cerevisiae*. *Microorganisms* **9**, 7 (2021).
68. Jacquier, A. Systems biology: supplementation is not sufficient. *Nat. Microbiol.* **1**, 16016 (2016).
69. Bianchi, F. et al. Asymmetry in inward- and outward-affinity constant of transport explain unidirectional lysine flux in *Saccharomyces cerevisiae*. *Sci. Rep.* **6**, 31443 (2016).
70. Alam, M. T. et al. The self-inhibitory nature of metabolic networks and its alleviation through compartmentalization. *Nat. Commun.* **8**, 16018 (2017).
71. Nogae, I. & Johnston, M. Isolation and characterization of the *ZWF1* gene of *Saccharomyces cerevisiae*, encoding glucose-6-phosphate dehydrogenase. *Gene* **96**, 161–169 (1990).
72. Ralser, M. et al. Dynamic rerouting of the carbohydrate flux is key to counteracting oxidative stress. *J. Biol.* **6**, 10 (2007).
73. Campbell, K., Vowinckel, J., Keller, M. A. & Ralser, M. Methionine metabolism alters oxidative stress resistance via the pentose phosphate pathway. *Antioxid. Redox Signal.* **24**, 543–547 (2016).
74. Grüning, N.-M. et al. Pyruvate kinase triggers a metabolic feedback loop that controls redox metabolism in respiring cells. *Cell Metab.* **14**, 415–427 (2011).
75. Celton, M. et al. A comparative transcriptomic, fluxomic and metabolomic analysis of the response of *Saccharomyces cerevisiae* to increases in NADPH oxidation. *BMC Genomics* **13**, 317 (2012).
76. Kim, D.-H. et al. mTOR interacts with raptor to form a nutrient-sensitive complex that signals to the cell growth machinery. *Cell* **110**, 163–175 (2002).
77. Epstein, C. B. et al. Genome-wide responses to mitochondrial dysfunction. *Mol. Biol. Cell* **12**, 297–308 (2001).
78. Traven, A., Wong, J. M., Xu, D., Sopta, M. & Ingles, C. J. Interorganellar communication. Altered nuclear gene expression profiles in a yeast mitochondrial DNA mutant. *J. Biol. Chem.* **276**, 4020–4027 (2001).
79. Ruzicka, F. J. & Beinert, H. The soluble 'high potential' type iron–sulfur protein from mitochondria is aconitase. *J. Biol. Chem.* **253**, 2514–2517 (1978).
80. Kispal, G., Csere, P., Prohl, C. & Lill, R. The mitochondrial proteins Atm1p and Nfs1p are essential for biogenesis of cytosolic Fe/S proteins. *EMBO J.* **18**, 3981–3989 (1999).
81. Kaut, A., Lange, H., Diekert, K., Kispal, G. & Lill, R. Isa1p is a component of the mitochondrial machinery for maturation of cellular iron–sulfur proteins and requires conserved cysteine residues for function. *J. Biol. Chem.* **275**, 15955–15961 (2000).
82. Chen, O. S., Hemenway, S. & Kaplan, J. Inhibition of Fe–S cluster biosynthesis decreases mitochondrial iron export: evidence that Yfh1p affects Fe–S cluster synthesis. *Proc. Natl Acad. Sci. USA* **99**, 12321–12326 (2002).
83. Gillet, L. C. et al. Targeted data extraction of the MS/MS spectra generated by data-independent acquisition: a new concept for consistent and accurate proteome analysis. *Mol. Cell. Proteomics* **11**, O111.016717 (2012).
84. Vowinckel, J. et al. The beauty of being (label)-free: sample preparation methods for SWATH–MS and next-generation targeted proteomics. *F1000Res.* **2**, 272 (2013).
85. Puig, S., Askeland, E. & Thiele, D. J. Coordinated remodeling of cellular metabolism during iron deficiency through targeted mRNA degradation. *Cell* **120**, 99–110 (2005).

86. Regev-Rudzki, N., Karniely, S., Ben-Haim, N. N. & Pines, O. Yeast aconitase in two locations and two metabolic pathways: seeing small amounts is believing. *Mol. Biol. Cell* **16**, 4163–4171 (2005).
87. Farooq, M. A., Pracheil, T. M., Dong, Z., Xiao, F. & Liu, Z. Mitochondrial DNA instability in cells lacking aconitase correlates with iron citrate toxicity. *Oxid. Med. Cell. Longev.* **2013**, e493536 (2013).
88. Chen, X. J., Wang, X., Kaufman, B. A. & Butow, R. A. Aconitase couples metabolic regulation to mitochondrial DNA maintenance. *Science* **307**, 714–717 (2005).
89. Chacinska, A., Koehler, C. M., Milenkovic, D., Lithgow, T. & Pfanner, N. Importing mitochondrial proteins: machineries and mechanisms. *Cell* **138**, 628–644 (2009).
90. Kohlhaw, G. B. Leucine biosynthesis in fungi: entering metabolism through the back door. *Microbiol. Mol. Biol. Rev.* **67**, 1–15 (2003).
91. Ljungdahl, P. O. & Daignan-Fornier, B. Regulation of amino acid, nucleotide, and phosphate metabolism in *Saccharomyces cerevisiae*. *Genetics* **190**, 885–929 (2012).
92. Tracy, J. W. & Kohlhaw, G. B. Reversible, coenzyme-A-mediated inactivation of biosynthetic condensing enzymes in yeast: a possible regulatory mechanism. *Proc. Natl Acad. Sci. USA* **72**, 1802–1806 (1975).
93. Irvin, S. D. & Bhattacharjee, J. K. A unique fungal lysine biosynthesis enzyme shares a common ancestor with tricarboxylic acid cycle and leucine biosynthetic enzymes found in diverse organisms. *J. Mol. Evol.* **46**, 401–408 (1998).
94. Winzeler, E. A. et al. Functional characterization of the *S. cerevisiae* genome by gene deletion and parallel analysis. *Science* **285**, 901–906 (1999).
95. Goldstein, A. L. & McCusker, J. H. Three new dominant drug resistance cassettes for gene disruption in *Saccharomyces cerevisiae*. *Yeast* **15**, 1541–1553 (1999).
96. Sikorski, R. S. & Hieter, P. A system of shuttle vectors and yeast host strains designed for efficient manipulation of DNA in *Saccharomyces cerevisiae*. *Genetics* **122**, 19–27 (1989).
97. Klinger, H. et al. Quantitation of (a)symmetric inheritance of functional and of oxidatively damaged mitochondrial aconitase in the cell division of old yeast mother cells. *Exp. Gerontol.* **45**, 533–542 (2010).
98. Motley, A. M. & Hettema, E. H. Yeast peroxisomes multiply by growth and division. *J. Cell Biol.* **178**, 399–410 (2007).
99. Baganz, F., Hayes, A., Marren, D., Gardner, D. C. & Oliver, S. G. Suitability of replacement markers for functional analysis studies in *Saccharomyces cerevisiae*. *Yeast* **13**, 1563–1573 (1997).
100. Schweiger, M. R. et al. Genome-wide massively parallel sequencing of formaldehyde fixed-paraffin embedded tumor tissues for copy-number and mutation analysis. *PLoS ONE* **4**, e5548 (2009).
101. Li, H. & Durbin, R. Fast and accurate short read alignment with Burrows–Wheeler transform. *Bioinformatics* **25**, 1754–1760 (2009).
102. Wang, K., Li, M. & Hakonarson, H. ANNOVAR: functional annotation of genetic variants from high-throughput sequencing data. *Nucleic Acids Res.* **38**, e164 (2010).
103. Kahm, M., Hasenbrink, G., Lichtenberg-Fraté, H., Ludwig, J. & Kschischo, M. grofit: fitting biological growth curves with R. *J. Stat. Softw.* **33**, 1–21 (2010).
104. Litsios, A. et al. Differential scaling between G1 protein production and cell size dynamics promotes commitment to the cell division cycle in budding yeast. *Nat. Cell Biol.* **21**, 1382–1392 (2019).
105. Lamprecht, M. R., Sabatini, D. M. & Carpenter, A. E. CellProfiler: free, versatile software for automated biological image analysis. *Biotechniques* **42**, 71–75 (2007).
106. Zelezniak, A. et al. Machine learning predicts the yeast metabolome from the quantitative proteome of kinase knockouts. *Cell Syst.* **7**, 269–283 (2018).
107. Mülleder, M. et al. Functional metabolomics describes the yeast biosynthetic regulome. *Cell* **167**, 553–565 (2016).
108. Mülleder, M., Bluemlein, K. & Ralser, M. A high-throughput method for the quantitative determination of free amino acids in *Saccharomyces cerevisiae* by hydrophilic interaction chromatography–tandem mass spectrometry. *Cold Spring Harb. Protoc.* **2017**, pdb.prot089094 (2017).
109. Szklarczyk, D. et al. STRING v11: protein–protein association networks with increased coverage, supporting functional discovery in genome-wide experimental datasets. *Nucleic Acids Res.* **47**, D607–D613 (2019).
110. Jassal, B. et al. The reactome pathway knowledgebase. *Nucleic Acids Res.* **48**, D498–D503 (2020).
111. MacRae, J. I. et al. Mitochondrial metabolism of sexual and asexual blood stages of the malaria parasite *Plasmodium falciparum*. *BMC Biol.* **11**, 67 (2013).
112. Behrends, V., Tredwell, G. D. & Bundy, J. G. A software complement to AMDIS for processing GC–MS metabolomic data. *Anal. Biochem.* **415**, 206–208 (2011).
113. Molik, S., Lill, R. & Mühlenhoff, U. Methods for studying iron metabolism in yeast mitochondria. *Methods Cell Biol.* **80**, 261–280 (2007).
114. Passonneau, J. V. & Lowry, O. H. in *Enzymatic Analysis* 229–305 (Humana Press, 1993); https://doi.org/10.1007/978-1-60327-407-4_7
115. Magri, S., Fracasso, V., Rimoldi, M. & Taroni, F. Preparation of yeast mitochondria and in vitro assay of respiratory chain complex activities. *Nat. Protoc.* https://doi.org/10.1038/nprot.2010.25 (2010).
116. Stock, D., Leslie, A. G. & Walker, J. E. Molecular architecture of the rotary motor in ATP synthase. *Science* **286**, 1700–1705 (1999).

Acknowledgements

We thank our laboratory members and J. Bähler for critical discussion and comments on the manuscript, and C. Kilian for technical support. This work was supported by the Francis Crick Institute, which receives its core funding from Cancer Research UK (FC001134), the UK Medical Research Council (FC001134) and the Wellcome Trust (FC001134), and received specific funding from the European Research Council (StG 260809 and SYG 951475) and the Wellcome Trust (IA 200829/Z/16/Z), as well as the FWF (Austria) for project P26713 (to M.B.) and a Swiss National Science Foundation Postdoc Mobility fellowship (191052 to J.H.).

Author contributions

J.V., J.H. and M. Ralser conceived the project, planned and designed experiments with input from all authors. M. Ralser supervised the project. J.V., J.H. and M. Ralser wrote the manuscript with help from all authors. J.V., J.H., H.M., M.K., K.R., M.A.K., M.M., J.D., M.W., M. Rinnerthaler, J.S.L.Y., S.K.A. and A.L. performed experiments and analysed the data. D.M., B.T., N.Z., C.D.D., J.I.M. and M.B. helped supervise the project and contributed to discussion and interpretation of the results.

Competing interests

The authors declare no competing interests.

Additional information

Extended data is available for this paper at https://doi.org/10.1038/s42255-021-00477-6.

Supplementary information The online version contains supplementary material available at https://doi.org/10.1038/s42255-021-00477-6.

Correspondence and requests for materials should be addressed to Markus Ralser.

Peer review information *Nature Metabolism* thanks the anonymous reviewers for their contribution to the peer review of this work. Primary Handling Editors: Ashley Castellanos-Jankiewicz; Pooja Jha.

Reprints and permissions information is available at www.nature.com/reprints.

Publisher's note Springer Nature remains neutral with regard to jurisdictional claims in published maps and institutional affiliations.

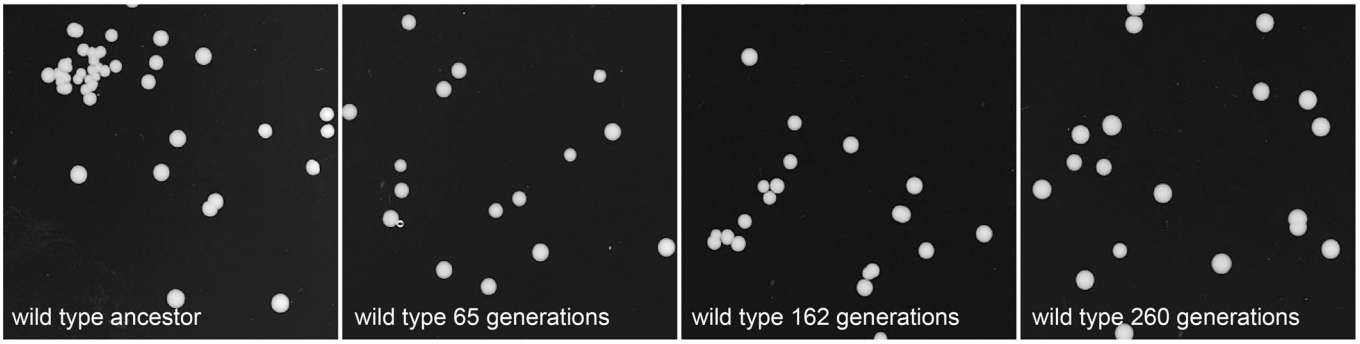

Extended Data Fig. 1 | Growth of wild-type strain is not affected by adaptive laboratory evolution. Wild-type yeast evolved in chemostats in parallel to corresponding petites that were sampled during the evolution experiment and spotted on solid F1 medium. Colony sizes remain largely unaffected over the course of the experiment. Shown is one of n = 3 biological replicates.

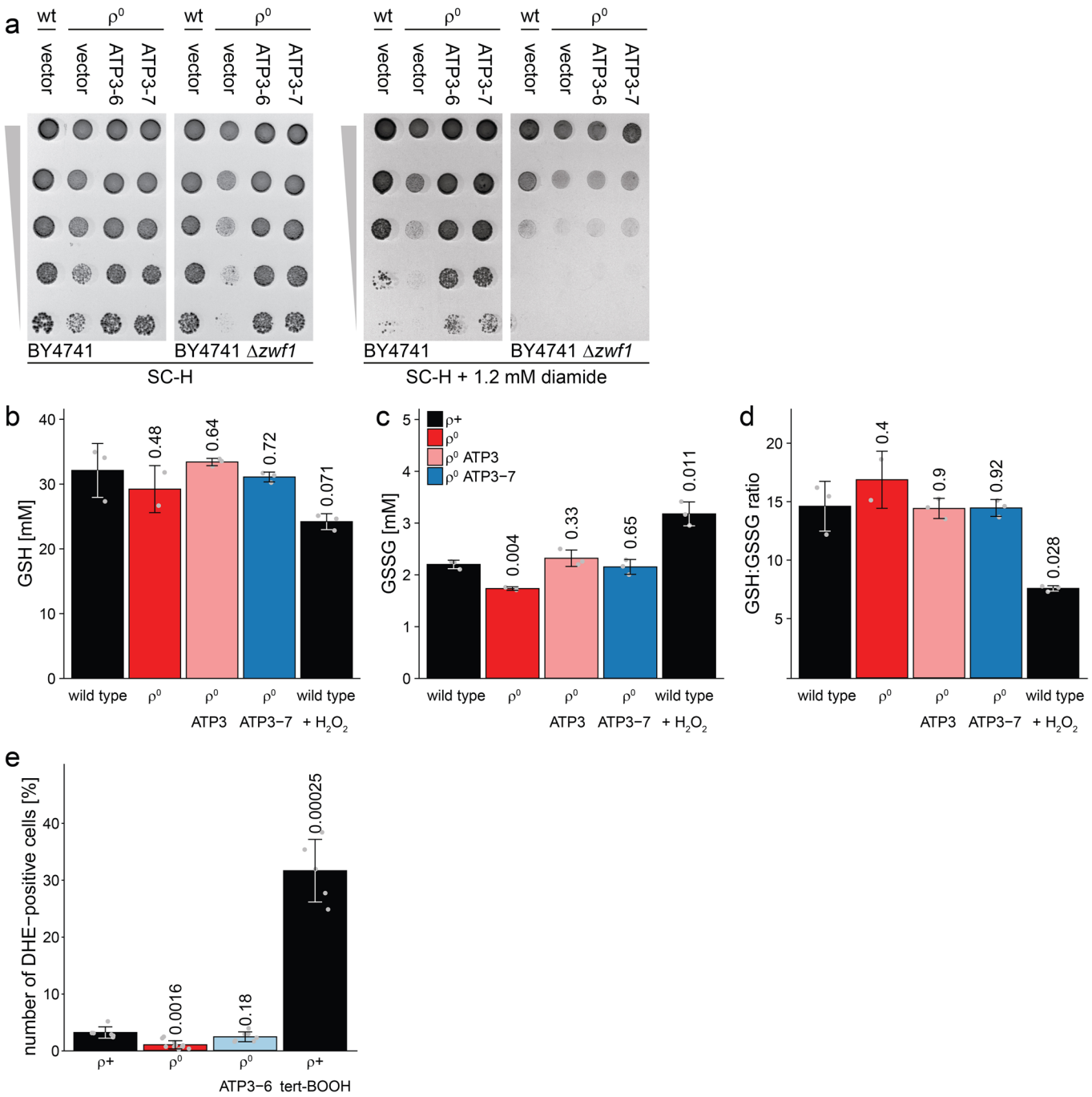

Extended Data Fig. 2 | Redox metabolism of wild-type, naive and evolved petites. a. Wild-type (ρ⁺) and petite (ρ⁰) BY4741 or BY4741 Δ*zwf1* yeast containing empty vector or plasmid-encoded *ATP3, ATP3-6* or *ATP3-7* were cultured in SC without histidine (SC-H) medium to mid-exponential phase, harvested, and spotted in serial dilutions onto freshly prepared SC-H agar plates ±the oxidant diamide (1.2 mM). Suppressor mutations (*ATP3-6*, *ATP3-7*) benefit growth in both BY4741 and BY4741 Δ*zwf1* background (left panel). Naive petites are slightly more sensitive to diamide compared to evolved petites and wild-type (right panel). In a Δ*zwf1* background, all strains are hypersensitive to diamide. Shown is one representative experiment n = 3 independent replicates. **b.-d**. Wild-type (ρ⁺) and petite (ρ⁰) YSBN11 strains containing empty vector or plasmid-encoded *ATP3, ATP3-6* or *ATP3-7* were cultured in SC-H medium to mid-exponential phase and reduced glutathione (GSH) and oxidized glutathione (GSSG) were quantified by LC-MS/MS. In comparison to untreated wild-type controls, treatment with H_2O_2 (0.5 mM) reduces GSH and increases GSSG levels (positive control). Instead, GSSG and GSH levels are largely unaffected in petites compared to wild-type. Statistics based on two-sided, unpaired t-tests of n = 3 biological replicates comparing wild type to other genotypes. Mean values ± SD. **e**. Wild-type (ρ⁺) and petite (ρ⁰) YSBN11 yeast containing empty vector or plasmid-encoded *ATP3-6* were cultured in SM medium, harvested in mid-log phase and re-suspended in medium ± 2 mM tert-BOOH. Superoxide levels were quantified by DHE oxidation after 5 min using fluorescence microscopy. 3 % of wild-type cells, 1 % of naive petite cells and 2 % of evolved petites show DHE fluorescence, while 31 % of wild-type cells challenged with tert-BOOH exhibit fluorescence. Statistics based on two-sided, unpaired t-tests of the following number of biological replicates comparing wild type to other genotypes ρ⁺, n = 6 replicates, 13260 cells; ρ⁰, n = 11 replicates, 14873 cells; ρ⁰ ATP3-6, n = 7 replicates, 17721 cells; ρ⁺ test-BOOH, n = 6 replicates, 17721 cells. Mean values ± SEM are shown.

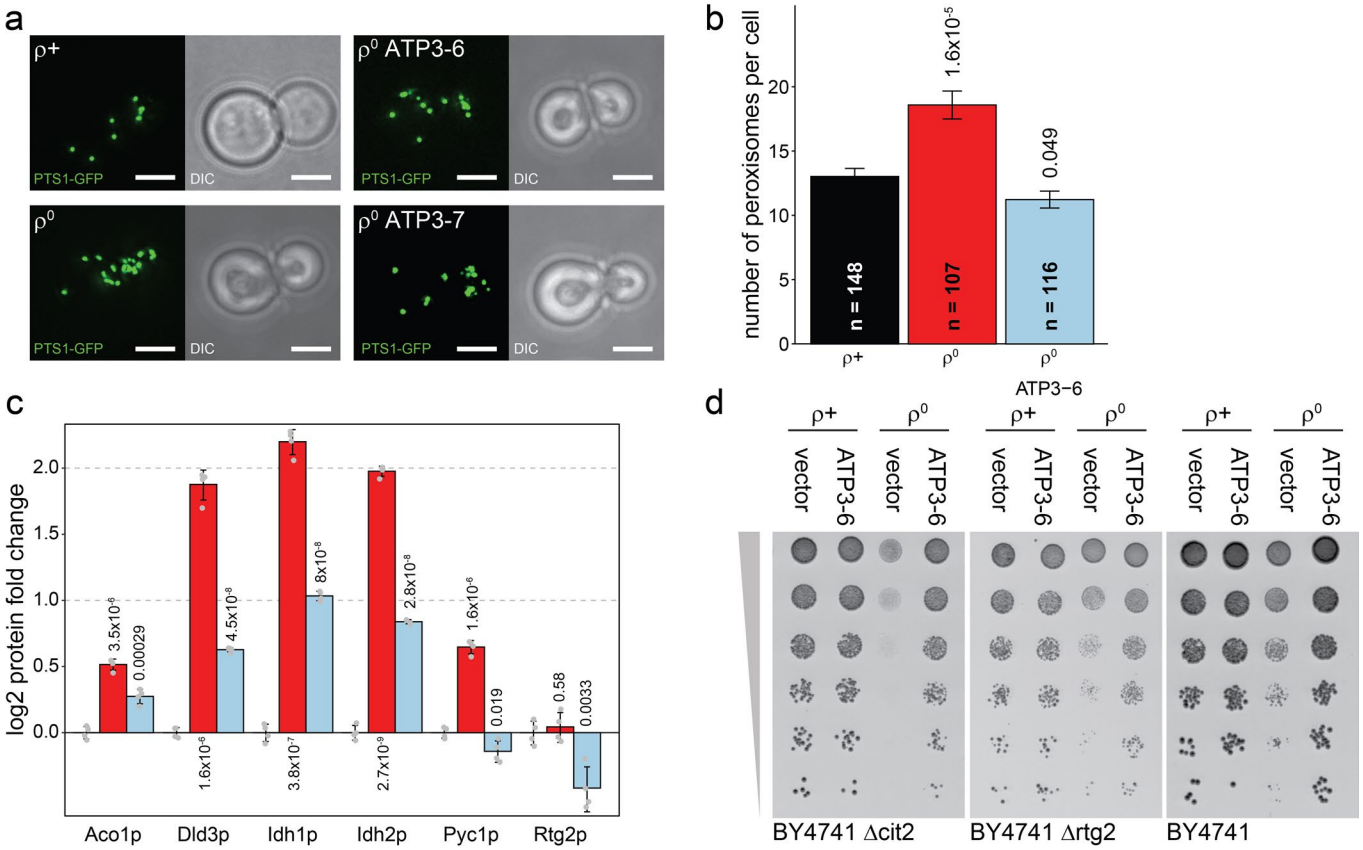

Extended Data Fig. 3 | Retrograde response is activated in petites, mitigated in evolved petites, but is not required for suppression of the petite phenotype. a., b., Wild-type (ρ⁺) and petite (ρ⁰) BY4741 strains containing empty vector or plasmid-encoded *ATP3-6* and *ATP3-7* variants were transformed with a plasmid encoding Pts1-GFP and cultured in SC-HU (histidin, uracil dropout) medium. Cells were harvested in mid-exponential growth phase, fixed with formaldehyde and observed by fluorescence microscopy. Dot-like structures represent peroxisomes (a). Scale bar = 1 µm. Compared to wild-type (10 ± 1) and evolved petites (10 ± 1), naive petites display a significant increase of peroxisomes (17 ± 1) (b). P-values shown based on unpaired, two-sided t-tests, comparing wild type to other genotypes. Mean values ± SEM. Number of cells quantified is indicated by n in the plot. **c**. Wild-type (ρ⁺) and petite (ρ⁰) YSBN11 yeast containing empty vector or plasmid-encoded *ATP3-6* were cultured in SM medium. In the mid-exponential growth phase, cells were harvested and subjected to a proteomics workflow. Shown protein fold-changes were normalized to the wild-type. Proteins previously described to be controlled by retrograde response (RTG)[1,61,77,78] as well as regulator Rtg2p are significantly upregulated in naive petites (empty plasmid). In comparison, up-regulation in the evolved petite (*ATP3-6*) is significantly less pronounced. Statistics based on two-sided, unpaired t-tests of n = 3 biological replicates comparing wild type to other genotypes. Mean values ± SD. **d**. *RTG2* or *CIT2* are not required for petite suppression. Wild-type (ρ⁺) BY4741 yeast and strains deleted for *RTG2* and *CIT2* were transformed with empty plasmid or plasmid encoding for *ATP3-6*, and mtDNA was depleted. Cells were grown to mid-log growth phase, and equal numbers were spotted in serial dilutions onto SC-H agar. Petites suffer from a growth defect compared to wild-type, which is further amplified in Δ*rtg2* and Δ*cit2* strains. Instead, expression of *ATP3-6* restores growth irrespective of the genetic background (wild-type, Δ*rtg2* and Δ*cit2*).

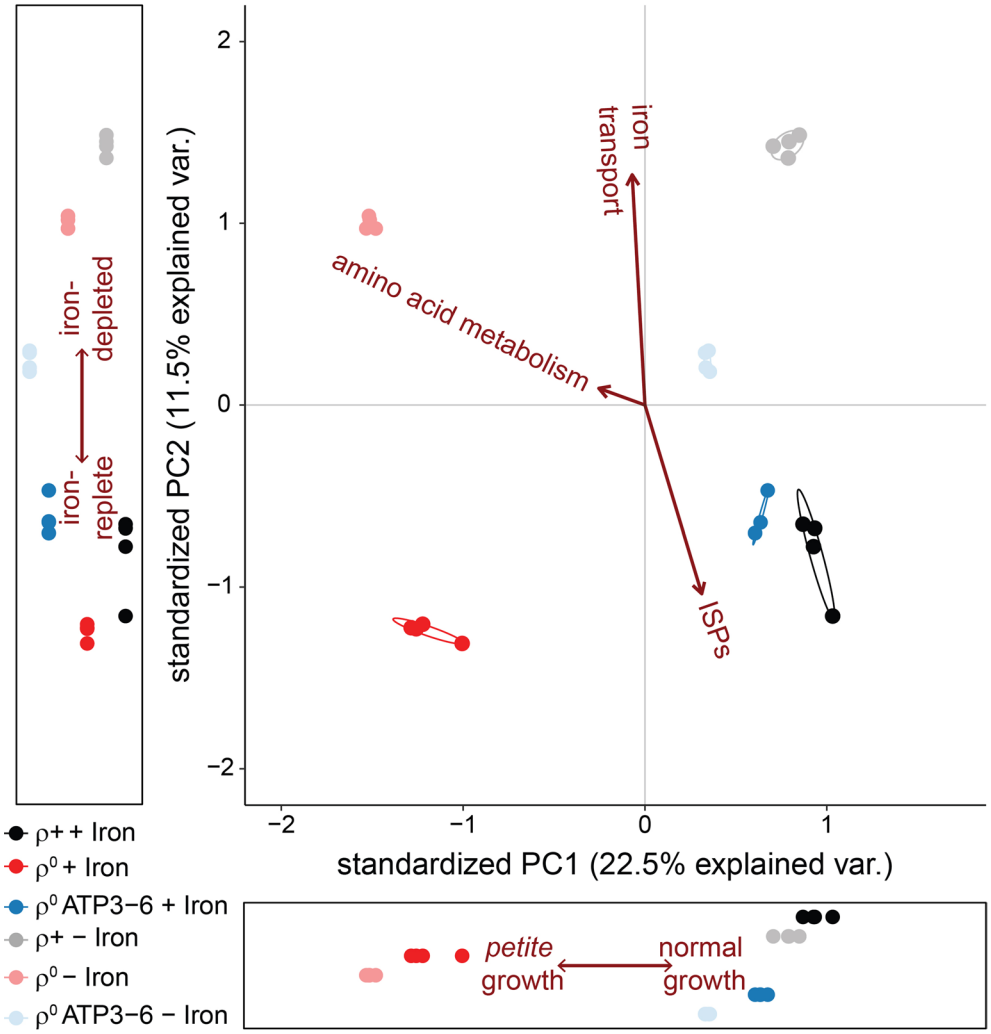

Extended Data Fig. 4 | Principal component analysis of proteome changes in response to iron depletion. Wild-type (ρ^+) and petite (ρ^0) YSBN11 strains containing empty vector or plasmid-encoded *ATP3-6* were cultured in iron-depleted SM medium (- iron) or SM medium containing 200 µg/L iron[III] chloride (+ iron). In the mid-exponential phase, cells were harvested, and proteins were extracted and trypsin-digested. Samples were analyzed by SWATH-MS and protein fold-changes were calculated in comparison to the iron-replete wild-type condition, and data was analyzed using principal component (PC) analysis. In PC1, proteomes were separated according to the petite (slow-growth) phenotype, with evolved petites (expressing *ATP3-6*) clustering with the wild-type. In PC2, iron-repleted yeast proteomes are separated from iron-depleted proteomes. Combined loadings of all proteins belonging to three GO term groups were plotted (red arrows), showing change of amino acid metabolism along PC1, and up-regulation of iron transport and down-regulation of iron-sulfur proteins (ISPs) along PC2. Data from n = 4 biological replicates per genotype.

nature research

Corresponding author(s): Markus Ralser

Last updated by author(s): 29082021

Reporting Summary

Nature Research wishes to improve the reproducibility of the work that we publish. This form provides structure for consistency and transparency in reporting. For further information on Nature Research policies, see our Editorial Policies and the Editorial Policy Checklist.

Statistics

For all statistical analyses, confirm that the following items are present in the figure legend, table legend, main text, or Methods section.

n/a	Confirmed	
☐	☒	The exact sample size (*n*) for each experimental group/condition, given as a discrete number and unit of measurement
☐	☒	A statement on whether measurements were taken from distinct samples or whether the same sample was measured repeatedly
☐	☒	The statistical test(s) used AND whether they are one- or two-sided *Only common tests should be described solely by name; describe more complex techniques in the Methods section.*
☒	☐	A description of all covariates tested
☐	☒	A description of any assumptions or corrections, such as tests of normality and adjustment for multiple comparisons
☐	☒	A full description of the statistical parameters including central tendency (e.g. means) or other basic estimates (e.g. regression coefficient) AND variation (e.g. standard deviation) or associated estimates of uncertainty (e.g. confidence intervals)
☐	☒	For null hypothesis testing, the test statistic (e.g. *F*, *t*, *r*) with confidence intervals, effect sizes, degrees of freedom and *P* value noted *Give P values as exact values whenever suitable.*
☒	☐	For Bayesian analysis, information on the choice of priors and Markov chain Monte Carlo settings
☒	☐	For hierarchical and complex designs, identification of the appropriate level for tests and full reporting of outcomes
☐	☒	Estimates of effect sizes (e.g. Cohen's *d*, Pearson's *r*), indicating how they were calculated

Our web collection on statistics for biologists contains articles on many of the points above.

Software and code

Policy information about availability of computer code

Data collection	Agilent Technologies Masshunter software suite B.07.00, Sciex Analyst 1.6, Tecan SparkControl 2.1, BMG Labtech Reader Control 2.20
Data analysis	Vector NTI 9.0 PlasmaDNA 1.4.2, MitoLoc (https://github.com/gurdon-institute/Yeast_MitoMap.git), Burrows Wheeler Alignment (BWA) 0.5.9-r16, GATK 2.2 ANNOVAR (Ensembl Saccharomyces cerevisiae v69), ImageJ 1.49, CellProfiler 2.0, FlowJo 10.6.2, StringDB 11, Softworx 6, Spectronaut 14, Pymol 2.0, Adobe Illustrator 2021 (CC), Microsoft Excel 2016-2020, R 4.0 (also see deposited code at github.com/JakobV/metabolic-growth-limitations-of-petite-cells)

For manuscripts utilizing custom algorithms or software that are central to the research but not yet described in published literature, software must be made available to editors and reviewers. We strongly encourage code deposition in a community repository (e.g. GitHub). See the Nature Research guidelines for submitting code & software for further information.

Data

Policy information about availability of data

All manuscripts must include a data availability statement. This statement should provide the following information, where applicable:

- Accession codes, unique identifiers, or web links for publicly available datasets
- A list of figures that have associated raw data
- A description of any restrictions on data availability

Proteomic data is provided in PRIDE under the accession number PXD011715. A list of mass spectrometry files is provided in Suppl. Table 5. Processed metabolomics and proteomics data are provided in Suppl. Data Tables 1 - 3. There is no restriction on data availability.

Field-specific reporting

Please select the one below that is the best fit for your research. If you are not sure, read the appropriate sections before making your selection.

☒ Life sciences ☐ Behavioural & social sciences ☐ Ecological, evolutionary & environmental sciences

For a reference copy of the document with all sections, see nature.com/documents/nr-reporting-summary-flat.pdf

Life sciences study design

All studies must disclose on these points even when the disclosure is negative.

Sample size	Results are based on replicated samples, and sufficient data points have been recorded to fulfill the requirements of the statistical tests used. No sample size calculation was performed, and number of replicates was chosen based on experience and previous publications/work applying similar methodologies.
Data exclusions	There was no data excluded from the analysis.
Replication	Three biological/independent replicates were usually performed for each experiment. Exceptions are listed in the figure captions, which detail all replicate numbers and the nature of replication.
Randomization	In analytical experiments, the samples were randomized. For other experiments, randomization was not applied, as they were either performed in parallel, or as we did not expect an influence of acquisition order on the outcome of the experiment as judged by experience and previous publications/work applying similar methodologies.
Blinding	Microscopy image acquisition was performed in such a way that the investigator was blinded for sample identity. For other experiments, knowledge of sample identity was not relevant, as data was acquired and/or processed in a way that did not require subjective interpretation.

Reporting for specific materials, systems and methods

We require information from authors about some types of materials, experimental systems and methods used in many studies. Here, indicate whether each material, system or method listed is relevant to your study. If you are not sure if a list item applies to your research, read the appropriate section before selecting a response.

Materials & experimental systems

n/a	Involved in the study
☒	☐ Antibodies
☒	☐ Eukaryotic cell lines
☒	☐ Palaeontology and archaeology
☒	☐ Animals and other organisms
☒	☐ Human research participants
☒	☐ Clinical data
☒	☐ Dual use research of concern

Methods

n/a	Involved in the study
☒	☐ ChIP-seq
☐	☒ Flow cytometry
☒	☐ MRI-based neuroimaging

Flow Cytometry

Plots

Confirm that:

☒ The axis labels state the marker and fluorochrome used (e.g. CD4-FITC).

☒ The axis scales are clearly visible. Include numbers along axes only for bottom left plot of group (a 'group' is an analysis of identical markers).

☒ All plots are contour plots with outliers or pseudocolor plots.

☒ A numerical value for number of cells or percentage (with statistics) is provided.

Methodology

Sample preparation	Following culture, staining with DIOC6 and washing with PBS, 200 ul of each culture was transferred to a U-bottomed 96 well plate and taken for high-throughput flow cytometry analysis on a Fortessa X20 HTS cytometer. Acquisition parameters were 120 ul sample injection at a flow rate of 1 ul/sec. DiOC6 fluorescence was captured using 488 nm blue laser excitation followed by a 530/30 bandpass filter.

Instrument	BD Fortessa X20B-HTS
Software	FlowJo (v10.6.2), R (4.0.2)
Cell population abundance	Not applicable as cells were only analysed and not sorted.
Gating strategy	A threshold exclusion of 5000 was set on the cytometer to omit debris. FSC-A vs SSC-A was then used to identify the main population. Double discrimination was performed using FSC-A vs FSC-H followed by SSC-A vs SSC-H. R. A negative control of cells treated without DIOC6 was included.

☒ Tick this box to confirm that a figure exemplifying the gating strategy is provided in the Supplementary Information.